crystals

MDPI

Review

Basic Concepts and Recent Advances of Crystallographic Orientation Determination of Graphene by Raman Spectroscopy

Yucheng Lan [1,*], Mobolaji Zondode [1], Hua Deng [2], Jia-An Yan [3], Marieme Ndaw [1], Abdellah Lisfi [1], Chundong Wang [4,*] and Yong-Le Pan [5]

1 Department of Physics and Engineering Physics, Morgan State University, Baltimore, MD 21251, USA; mozon1@morgan.edu (M.Z.); manda2@morgan.edu (M.N.); abdellah.lisfi@morgan.edu (A.L.)
2 Department of Chemistry, Morgan State University, Baltimore, MD 21251, USA; hua.deng@morgan.edu
3 Department of Physics, Astronomy, and Geosciences, Towson University, Towson, MD 21252, USA; jyan@towson.edu
4 School of Optical and Electronic Information, Huazhong University of Science and Technology, Wuhan 430074, China
5 U. S. Army Research Laboratory, Adelphi, MD 20783, USA; yongle.pan.civ@mail.mil
* Correspondence: yucheng.lan@morgan.edu (Y.L.); apcdwang@hust.edu.cn (C.W.)

Received: 30 April 2018; Accepted: 19 September 2018; Published: 21 September 2018

Abstract: Graphene is a kind of typical two-dimensional material consisting of pure carbon element. The unique material shows many interesting properties which are dependent on crystallographic orientations. Therefore, it is critical to determine their crystallographic orientations when their orientation-dependent properties are investigated. Raman spectroscopy has been developed recently to determine crystallographic orientations of two-dimensional materials and has become one of the most powerful tools to characterize graphene nondestructively. This paper summarizes basic aspects of Raman spectroscopy in crystallographic orientation of graphene nanosheets, determination principles, the determination methods, and the latest achievements in the related studies.

Keywords: graphene; orientation; Raman; review

1. Introduction

When three-dimensional (3D) materials are reduced to two dimensional materials (2D), such as to nanosheets with several atomic layers, the produced 2D materials can exhibit unique properties and phenomena which are distinct from their 3D counterparts [1–4]. Up to now, many kinds of 2D materials have been produced and investigated, such as transition metal dichalcogindes [1,5], black phosphorus crystals [6–8], boron nitride nanosheets [9,10], molybdenum disulfide nanosheets [11], 2D topological insulators [12,13], graphitic carbon nitride nanosheets [14], and so on [15–17]. These 2D materials show unique physical and chemical properties and attract more and more attentions. Among them, graphene is the first 2D material that has been widely investigated [18,19]. Many interesting phenomena and novel applications have been reported, such as the quantum Hall effect [20–23]. Up to date, graphene becomes a promising candidate for fundamental studies [22–24] as well as for potential device applications [25–32]. Their excellent mechanical and electrical properties are strongly orientation-dependent. Additionally, their unique superconductivity [33,34], ferromagnetism [35], and quantum Hall effect [36] are related to their localized edge states too, being orientation-dependent. Thus, determination of the crystallographic orientation of graphene is essential in order to further understand these phenomena.

Up to now, various techniques have been developed to determine the crystallographic orientation of graphene, such as transmission electron microscopy [37–39] and selected-area electron diffraction [39,40], scanning electron microscopy [39,41], anisotropic optical absorption [42], high-resolution scanning tunneling microscopy [43–45], and so on. Among these techniques, Raman spectroscopy is a nondestructive, fast, and powerful technique to collect structural and electronic information of graphene. For example, Raman scattering has been utilized as an important tool to study physical properties of graphitic materials [46–48] and graphene nanosheets [49] over the last four decades. Until now, Raman spectroscopy has been an effective technique to nondestructively characterize graphene, detecting dopants [50–53], number of layers [49,54,55], linear dispersion of electronic energy [56], crystal orientation [57,58], defects [59], disorder [60], and strain [61,62] of graphene. The Raman spectroscopy of graphene has been reviewed [63–67] as well as scattering mechanisms [67,68]. Here, we focus on the applications of Raman spectroscopy on orientation determination of graphene nanosheets.

2. Raman Scattering of Graphene

Graphene is a two-dimensional single-atom-thick allotrope of carbon with a honeycomb structure, as shown in Figure 1. Due to the sp^2 hybridization of carbon bonds, carbon atoms arrange in a planar sheet, being bonded to three neighboring atoms.

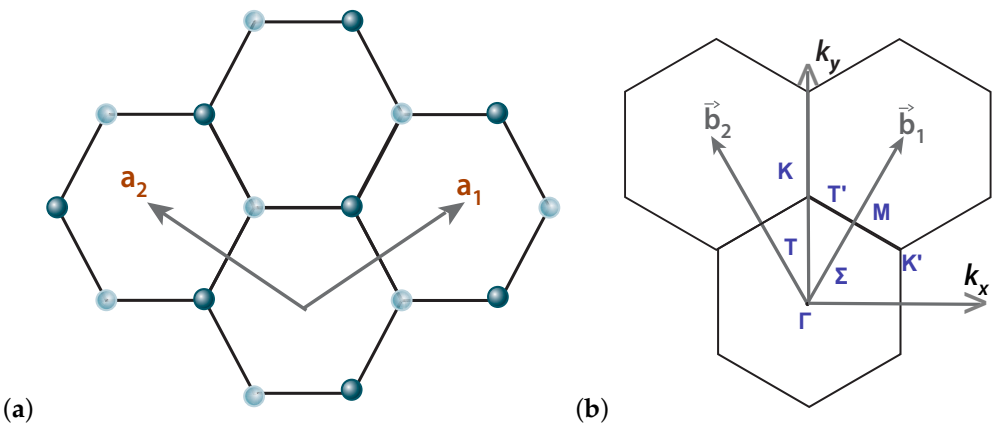

Figure 1. (**a**) Top view of monolayer graphene showing the inequivalent atoms A and B and the unit vectors $\vec{a}_1$ and $\vec{a}_2$ ($a_1 = a_2 = 2.4589$ Å at 297 K [69]). (**b**) The reciprocal space unit cell showing the first Brillouin zone (BZ) with its high-symmetry points and lines. The two primitive vectors, k_x and k_y, are the reciprocal space coordinate axes.

Figure 2 shows six phonon-dispersions of graphene. The iLO and iTO phonons are responsible for the main Raman bands observed in graphene. According to the group theory, these two modes are the only Raman active modes, corresponding to the two-dimensional E_{2g} phonon. The G band corresponds to the doubly degenerate E_{2g} modes at the Brillouin zone center Γ-point while D and $2D$ band to the Brillouin K-point [60,67].

Figure 3 shows a typical Raman spectrum of crystalline graphene on a SiO_2/Si substrate measured under 514.4 nm excitation. The Raman spectrum of carbon-based materials, including graphite and carbon nanotubes, is usually characterized by Raman-active modes from 800 cm^{-1} to 2000 cm^{-1}. Among these modes, the so-called D band locates around 1330–1360 cm^{-1} and the G band near 1580 cm^{-1} [60,63,67]. The Raman spectrum of crystalline monolayer graphene nanosheets is mainly dominated by two Raman bands, one at 1580 cm^{-1} and another at 2700 cm^{-1}. The band at 1580 cm^{-1} is intense and termed as the G band as in other carbon-based materials. Another band at 2700 cm^{-1} was historically termed the G' band [70], and is now termed as the $2D$ band [49] because the band is the overtone (second order) of the D band. The intensity of the $2D$ band depends on the number

of graphene layer, being roughly four times of that of the *G* band [49,55,71] for crystalline graphene nanosheets with single-layer atoms.

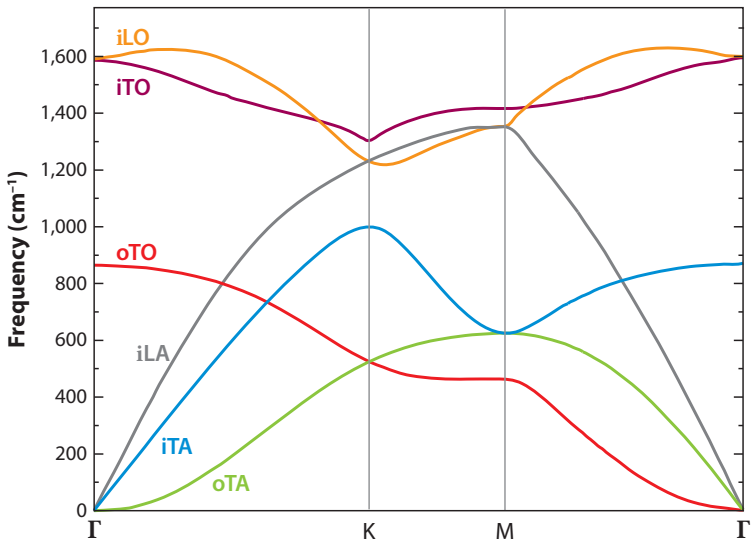

Figure 2. Calculated phonon dispersion relation of graphene showing the iLO, iTO, oTO, iLA, iTA and oTA phonon branches. i: in-plane; o: out-of-plane; A: acoustic; O: optical; T: transverse; L: longitudinal. (adapted from Reference [66,67]). The American Physical Society.

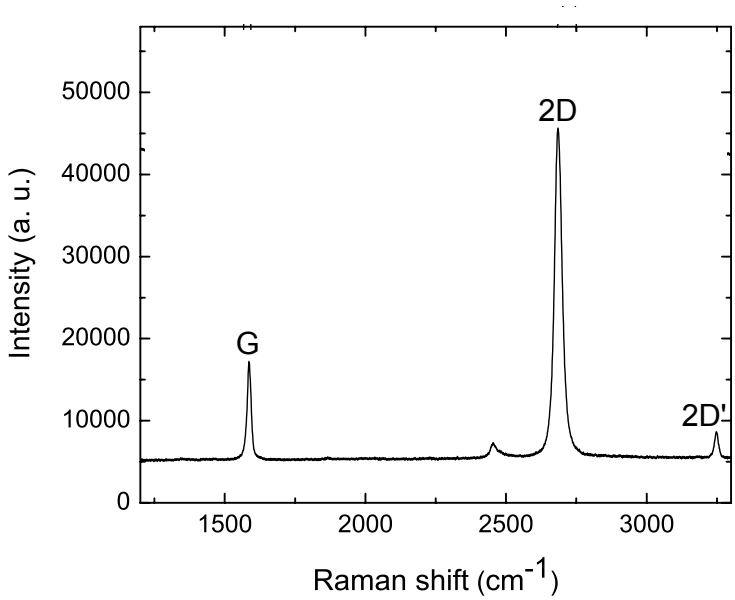

Figure 3. Raman scattering of crystalline graphene [49]. The American Physical Society.

The *D* band is very weak for crystalline graphene nanosheets and can only be observed in graphene nanosheet with defects. The $2D'$ band is observed sometimes. The details of these Raman bands (D, G, $2D$, and $2D'$) are discussed below.

2.1. G Band

Only first-order Raman bands are permitted for graphene because of the hexagonal symmetry of the graphene lattice (Figure 1a). There are two atoms in the unit cell of graphene, resulting in three zone-centered Raman modes. Two Raman modes, degenerating with E_{2g} symmetry with in-plane vibrations, are Raman active and responsible for the *G* band of graphene [60,67]. The third vibration

mode with B_{2g} symmetry is not Raman active. The *G* band, shown in Figure 3, is the main first-order Raman-active band in graphene nanosheets.

It is generally considered that the *G* band originates from the phonons at the center of the first Brillouin zone, existing in all sp^2-hybridized carbon materials. Figure 1b shows the Γ points of the Brillouin zone and Figure 4a shows two kinds of atom vibration modes of the Raman mode. The sp^2-hybridized carbon atoms vibrate in rings and chains. More detailed physical explanations of the *G* band is reviewed in the published literature [63].

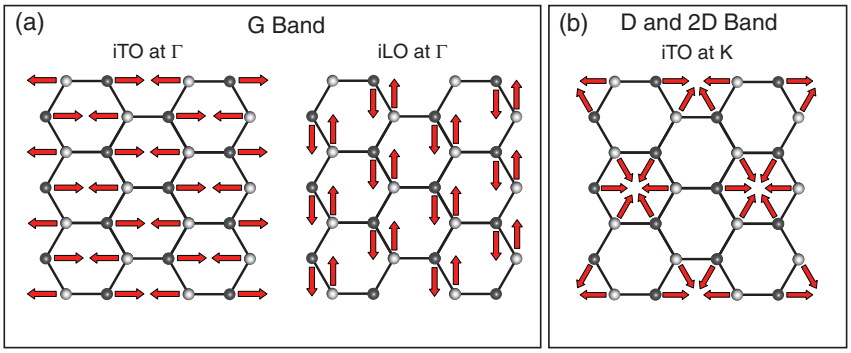

Figure 4. Phonon vibrations of Raman-active modes of graphene [72]. (**a**) *G* band vibration modes of the iTO and iLO phonons at the Γ-point. (**b**) *D* band vibration mode of the iTO phonons at the *K*-point. Wiley-VCH Verlag GmbH.

The two in-plane *G* modes shown in Figure 4a are doubly degenerated as TO phonon modes and LO phonon modes (with E_{2g} symmetry) at the Brillouin zone center [60]. The degeneracy can be destroyed by strains, splitting the *G* band into the G^+ and G^- bands. Therefore, the width of the *G* band have been employed to characterize the deformation and strain of graphene nanosheets [58]. The splitting has been also used to determine the crystallographic orientation, as discussed below.

The intensity of the *G* band depends on the the graphene thickness, linearly increasing with the increasing thickness because of detectable carbon atom quantities. Based on this phenomena, the intensity of the *G* band has been employed to determine the layer numbers of graphene nanosheets. One should keep in mind that the intensity of *G* band is also affected by annealing conditions [73] and the frequency of the *G* band is temperature dependent [74]. So it should be used carefully for the identification of number of the graphene layers because of the thermal effect. Therefore, a weak laser beam should be employed during Raman measurements to avoid potential thermal effects.

The *G* band is sensitively affected by strains [57,58,75,76]. More investigations indicated that the Raman frequency of the *G* band is affected by doping too [63,77–80] besides strains. The *G* band peak shifts with electron and hole doping concentrations [63,77].

2.2. 2D Band

The 2*D* band is usually the strongest Raman peak in graphene Raman spectrum, locating near 2700 cm^{-1}. This band was originally named the G' band [70,81] and denoted as G^* band in some literature [82]. In recent years, the band has been termed as the 2*D* band [49] because the Raman-active band is the result of a second order process of the *D* band, involving two phonons. Specifically the 2*D* Raman band is the overtone of the *D* band, which comes from the in-plane vibrational mode of the carbon rings (as shown in Figure 4b). The *D* band is related to the symmetry at the *K* or K' point of the first Brillouin zone, which are shown in Figure 1b. For the 2*D* vibrational band, the electrons will be scattered back to *K* point of the Brillouin zone before recombining with the hole, and then back-scattered by a second iTO phonon. This process is also known as the double resonance [49,81,83], because the incident electrons and the first scattered phonons are resonant in the graphene, or the scattered phonons are in resonant with the second scattered phonons. In the resonance procedures,

both the electrons and phonons are scattered by iTO phonons (coming from the K point) to the K' point, and then recombine to emit photons. More details of the 2D band were reviewed recently [84].

The 2D peak of single-layer graphene can be fitted with a Lorentzian function while the peak broadens/blue-shifts with increasing thickness of graphene [49,81]. The 2D peak of multilayer graphene are usually fitted with multiple peaks because the electronic band structure of the multilayer nanosheets are split [81]. For example, the 2D peak of a bi-layer graphene can be fitted by four Lorentzian peaks. Therefore, the 2D band has been used to determine the layer-numbers of graphene nanosheets experimentally [49] because of the thickness-dependence of the shape and width of the 2D band peak. The single-layer graphene can be detected simply and efficiently from the existence of a single/sharp 2D band peak [49].

The charge transfer would alter the equilibrium lattice parameter of graphene, resulting in a 2D band red-shifting with electron doping concentrations and a blue-shifting with hole doping concentration [52,79,80]. The 2D band is also affected by strains [57,58,75,76,85,86] and substrates [87,88]. When graphene is grown on substrates, the interaction between graphene and substrates can alter the position of the 2D mode. For example the 2D mode of graphene grown on copper substrates [87] is different from that grown on SiC [88] substrates, significantly influencing the determination of the number of graphene layers. Therefore, one should be careful to determine the number of graphene layers in Section 3.2.1.

2.3. D Band

The D band is another important Raman band of graphene, locating near 1350 cm^{-1}. The band comes from the disorder of graphene. The D mode associates with the transverse optical (TO) phonons around the K-point of the Brillouin zone [63]. Figure 4b shows the breathing mode of the band. The carbon atomic rings vibrate radially [89–91]. The D peak is usually very intense in amorphous carbon isotropies while absent in perfect graphitic materials. It should be noticed that I_D/I_G increases with the defect density only at low defect density region because of more elastic scattering but decreases with the increasing defect density at high defect density region because of attenuating Raman peaks [63,92–94]. The strong D bands are visible only for high sp^2/low sp^3 amorphous carbon [93,94]. Therefore it should be careful to detect the defect density from I_D/I_G ratio.

Its overtone band is the 2D band, locating near 2660–2710 cm^{-1}. Different from the D band, the 2D band is always visible even when the D band is very weak.

The D mode comes from defects [90] and is attributed to an A_{1g} zone-boundary mode [89]. Any defects disrupting the symmetry of graphene lattices can induce the D mode. In the case of the perfect amorphous carbon, there is a strong D band. The D mode appears when the carbon hexagons were destroyed. In other words, the D band disappears when the carbon honeycomb structure is perfect. Therefore, the low intensity of D band together with the presence of 2D bands are a indicator of high quality graphene layer. More detailed physical explanations of the D band have been reviewed in literature [63,95] and discussed theoretically [96]. Interested readers are referred to the literature cited therefore.

Moreover, doping can also affect Raman shifts of G and 2D bands [52,63,79,80] besides strain. Additionally, substrates including SiO_2 usually shifts 2D peak significantly due to different interaction between graphene and substrates [87,88].

It should be mentioned that the 2D band of amorphous carbon is very weak while D band is strong. The intensity of 2D band increases with crystallinity of carbon materials while that of D band decreases. The D band almost disappears in crystalline graphene nanosheets without defects. The ratio of the two intensity (I_{2D}/I_D) indicates the crystallinity quality of graphene nanosheets.

Graphene edges are one kind of one-dimensional defects. The D band intensity is anisotropic along straight graphene edges, Theoretically the resonance process cannot occur for any arbitrary pair of electron along k vectors [97,98]. It is believed that the edge defects of graphene are completely delocalized along a direction *parallel* along the edges in its real space and the associated vectors are

completely delocalized along a direction *perpendicular* to the graphene edges in its reciprocal space. Therefore, straight edge defects have one-dimensional characters and can only transfer momentum in a direction perpendicular to the edges, showing anisotropy.

There are two kinds of edges in graphene, arm-chair edges and zigzag edges. The intensity of the D band strongly depends on the type of the edges [43]. The D band intensity is stronger at an armchair edge and is dependent on the laser light polarization [99]. The intensity is maximum when the laser light is parallel to the arm-chair edges [43,100]. In other words, the D band intensity is higher at armchair edges than that at zigzag edges. So, the edge chirality of graphene nanosheets can be detected from analyzing the D band intensity [97]. Below we'll discuss how to detect the crystallographic orientation of graphene from the D band intensity.

2.4. D' Band and $2D'$ Band

The D' band is induced by disorder in graphene [70], locating at 1620 cm^{-1}. The origin of the band is similar to that of the D band except that the related phonons are in the vicinity of the Γ point, not the K point of the Brillouin zone. The D' band intensity is same for both two types of edges while strongly dependent on types of defects in graphene [101]. The D' peak also shifts with the graphene thickness [55].

The $2D'$ band, overtone of the D' band, is also observed in some cases.

2.5. Effects of Functional Groups

Chemical functionalization offers a feasible method to alter the graphene's properties including mechanical, electronic and vibrational properties, affecting Raman bands. Graphene oxide (GO) [102–106], hydrogenated graphene [107] (graphane) and halogenated graphene (CX_m, X = F, Cl, Br, or I) [108] are typical graphene derivatives. The functional groups on the carbon nanosheet induce transitions of carbon atoms from sp^2 to sp^3 hybridization. They often significantly change the atomic structure of graphene and hence their mechanical and vibrational properties. Density functional theory calculations showed that the 2D Young's modulus of the armchair and zigzag configurations of both GO and graphene fluoride are about 2/3 the experimental value of graphene [108,109].

Evolution of the Raman spectra for functionalized graphene is strongly dependent on the species and coverage of the functional groups on the surface. As more functional groups adsorb on graphene, the sharp G peak at 1580 cm^{-1} becomes broadened, while the D peak at around 1350 cm^{-1} becomes more evident because of defects [110,111]. In graphene fluoride, the resonant $2D$ peaks at about 2600 cm^{-1} completely disappear after graphene is fully fluorinated. Similar broadening occurs for the G and and D band in graphene fluoride [106,108].

3. Procedures of Orientation Determination

3.1. Preparation of Graphene

Graphene has been prepared by various methods [112,113]. Up to present, several kinds of successful approaches developed to generate graphene, include but are not limited to micromechanical cleavage of graphite [20,114], epitaxial growth on substrates [28,115–120], chemical exfoliation [118,121,122], and electrochemical exfoliation [123–126]. The mechanical cleavage method can produce high-quality graphene nanosheets that are comparable to crystalline graphite while the production ratio is low. Epitaxially grown graphene is suitable for large area fabrication and is compatible with current Si processing techniques while the quality of produced graphene is not good as that of micromechanically cleaved graphene. Chemical exfoliation always produce lots of defects in graphene while massive graphene nanosheets can be produced in a short time.

3.2. Optical Observation of Graphene

Graphene is always optically examined under optical microscopes before the orientation of graphene nanosheets is determined by Raman scattering. With the development of detection techniques, graphene layers can be distinguished/isolated on oxidized Si wafers under optical microscopes based on optical contrast/interference [20,127–131].

In details, the graphene nanosheets can be transferred onto a Si wafer with SiO_2 film. The thickness of the SiO_2 layer is usually 300 nm [19,22]. The graphene can then be founded by naked eyes under an optical microscope because of interference between graphene and the SiO_2 layer. Graphene can be also visualized on Si with other thicknesses of SiO_2 if suitable filters are chosen [127]. In order to see the details of graphene, an optical microscope with a 100× and 0.9 numerical aperture (N. A.) objective is usually employed. Figure 5a shows a typical optical image of graphene nanosheets with various layers. The color of graphene varies, depending on their layer thickness.

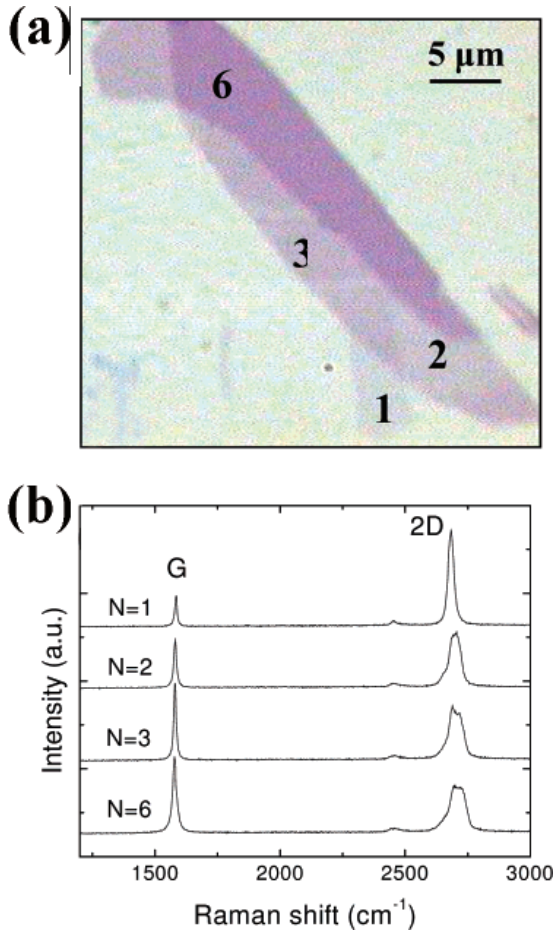

Figure 5. (**a**) Optical micrograph and (**b**) Raman spectra of multi-layered graphene with 1, 2, 3, and 6 layers [129]. The American Chemical Society.

3.2.1. Determination of Layer Number

The number of graphene layers can be estimated using optical contrast under optical microscopes. As shown in Figure 5a, single-layered graphene, double-layered graphene, and triple-layered graphene show different colors because of interference. A certain-layered graphene can be chosen from colors in experiments.

The layer number of graphene can be also measured from Raman spectra. As shown in Figure 5b, the *G* band intensity increases and its peak shifts with increasing layer numbers. The intensity ratio

I_{2D}/I_G is higher for few-layer graphene. The width of the 2*D* band increases with increasing layer numbers too. So the layer number of graphene can be estimated from the *G* band and the 2*D* band.

In addition to the Raman spectroscopy and traditional optical microscopy, the graphene layer numbers can be accurately identified by the contrast spectroscopy [54]. The number of layers (up to 10 layers) of a graphene sheet, which is deposited on a 300 nm SiO_2/Si substrate, can be precisely determined by using an equation of $C = 0.0046 + 0.0925N - 0.00255N^2$, where N is the number of layers of graphene and C is a contrast.

3.2.2. Estimation of Edge Chirality

Mechanically exfoliated graphene usually have certain orientation cleaved edges as well as CVD-grown graphene nanosheet. There are armchair edges or zigzag edges in most of graphene [37,132]. Therefore, the crystallographic orientation of graphene can be estimated from the crystallographic properties of graphene under optical microscopes, similar to ReS_2 nanosheets [133,134].

Figure 6a shows the crystallographic directions that form armchair edges and zigzag edges. An armchair edge is separated by an angle $\theta = (2n + 1) \times 30°$ with an adjacent zigzag edge, or by an angle of $\theta = 2n \times 30°$, where n is an integer. Therefore, graphene sheets usually have angles of $m \times 30°$ between two adjacent edges (one is armchair and another is zigzag), where m is an integer. Figure 6b illustrates several schematic graphene with armchair edges and zigzag edges, typically forming 30°, 60°, and 90° respectively. According to the crystallographic structures, two adjacent edges should have different chirality (one is armchair and the other is zigzag) when the angle between them is 30°, 90°, and 150°. Contrarily, both edges should have the same chirality (either armchair or zigzag) when the angle is 60° and 120°.

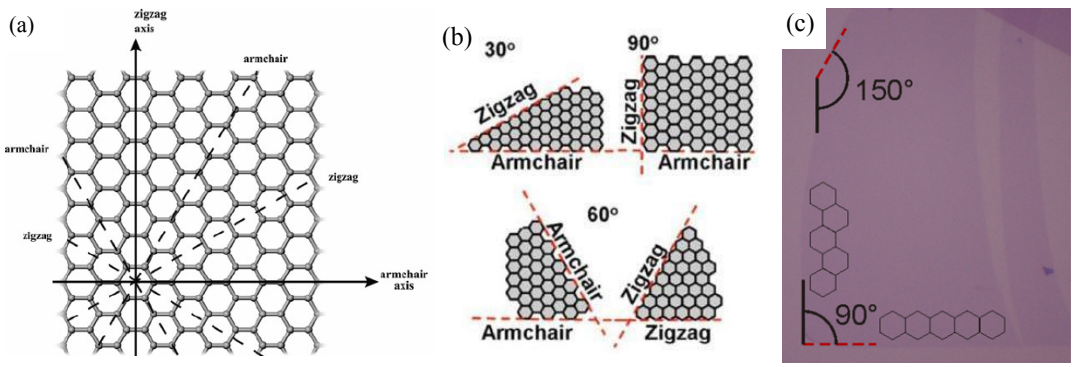

Figure 6. (**a**) Crystallographic directions giving rise to armchair and zigzag edge shapes [135]. (**b**) Schematic graphene edges. (**c**) Optical image of a graphene [44]. The American Physics Society.

Experimentally, the angle of adjacent edges can be measured under optical microscopes. Therefore same or different chirality of these adjacent edges can be judged simply from the optical angle observations, without knowing exactly which edges are armchair edges or zigzag edges.

Figure 6c shows a reported graphene sheet with one angle of 90° between two adjacent edges, and another is 150°. From above discussions, these adjacent edges should have the same chirality.

As the second step of the orientation determination, it is very useful to optically choose graphene nanosheets with a certain chirality under optical microscopes. Combined with traditional Raman scattering measurements, a graphene nanosheet with a number of layers and a morphology can be isolated under optical microscopes for further crystallographic orientation determinations.

3.3. Polarized Raman Spectroscopy

Polarized Raman scattering has been employed to determine crystallographic orientations from the 1980s [136–139] with an accuracy of ±2°. In recent years the technique has been used to determine

the orientation of graphene and other 2*D* materials. The detailed experimental procedures and principles are talked about below.

3.3.1. Experimental Setup

Figure 7 shows a typical experimental set up of polarized Raman spectroscopy [140]. An Ar-ion laser (wavelength $\lambda = 514.5$ nm) is usually used as an excitation source. A 40× microscope objective (N. A. = 0.6), or higher, is used to focus the laser beam onto graphene and to collect the scattered photons in a backscattering geometry. The scattered photons are dispersed with a grating of 1200 grooves/mm and detected by a liquid-nitrogen-cooled CCD detector. The spatial resolution of the microscope is less than 1 μm and the spectral resolution of the Raman system is $\sim$1 cm^{-1}.

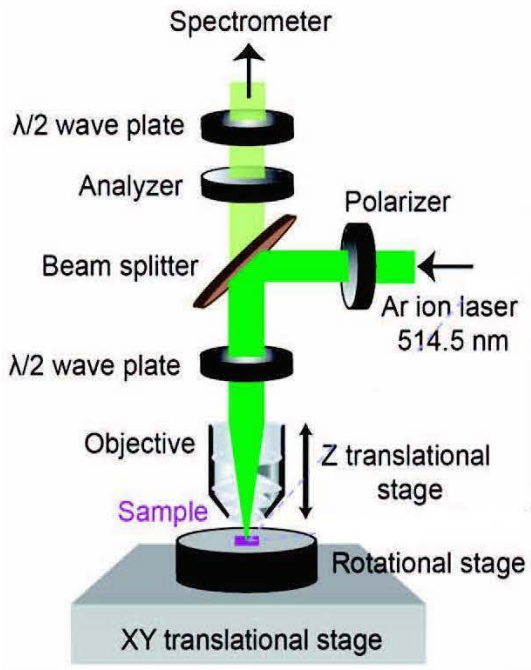

Figure 7. Schematic diagram of an experimental setup with a backscattering geometry [140]. The American Chemical Society.

When polarized Raman measurements are carried out, a half-wave plate is employed to rotate the polarization of the incident laser beam. A polarizer is used to align the polarization of the incident laser beam. Another linear polarizer is used as an analyzer for the scattered light to align the polarization of the scattering light into the spectrometer, perpendicular to the groove direction of the grating. A rotation sample stage is usually employed to rotate graphene too.

Figure 8 shows two polarization configurations in a polarized Raman spectroscopy. The polarization of the incident laser beam is chosen as a vertical polarization (V) direction or horizontal polarization (H), making a angle θ between the graphene plane and the laser beam. $\theta = 0°$ when the polarization is parallel to the surface of graphene planes. Figure 8b shows the in-plane configuration and the out-of-plane configuration in details, denoting by (VV) and (HH) configurations respectively.

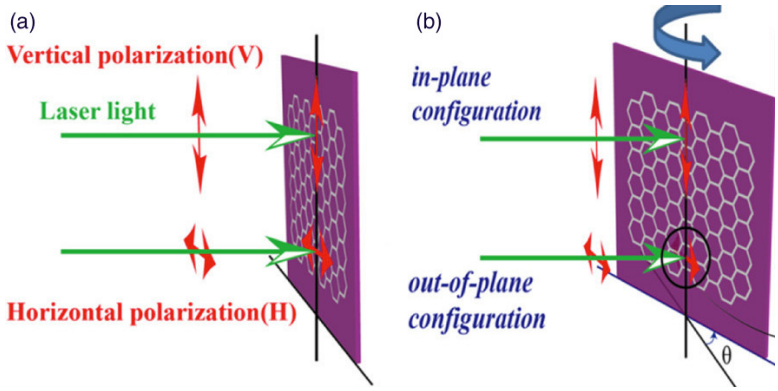

Figure 8. Polarization configurations in polarized Raman spectroscopy [141]. (**a**) Normal laser incidence ($\theta = 0$). Both the vertical polarization (VV) and the horizontal polarization (HH) of the laser light are parallel to the graphene plane. (**b**) Oblique laser incidence ($\theta \neq 0$). The vertical polarization is parallel to the graphene plane (top, in-plane configuration) and the horizontal polarization is not parallel to the graphene plane (bottom, out-of-plane configuration). Springer.

3.3.2. Raman Scattering Measurements

Raman spectra of the graphene can be collected for different polarization configurations. In a typical procedure to determine the crystallographic orientation of graphene, the incident polarization direction is fixed and the graphene sample is rotated using a rotation stage. The analyzer is fixed to cross polarization configuration (perpendicular to incident polarization). The graphene nanosheets are inspected first using the optical microscope in cross polarization. Rotating the graphene nanosheets until the graphene nanosheets become dark, the zigzag direction can then be determined in parallel or perpendicular to the incident polarization or the analyzer direction. At this step, the principal axe of the nanosheets can be detected although one cannot know it is the zigzag direction or armchair direction. The incident laser is then focused on the center of the graphene nanosheets and the polarization direction is aligned along the nanosheet edges (The polarization of the incident laser is tuned by rotating the half-wave plate). Raman spectra are then collected under various polarization of the analyzer. From the relationship between Raman peaks and the polarization angle, the armchair edge or zigzag edge can be detected, as discussed below. Similar procedures have been employed to determine an orientation of other 2*D* material nanosheets, such as black phosphorus [142].

4. Orientation Determination from Raman Spectroscopy

Some Raman bands of graphene are dependent on crystallographic orientation as well as their strain-dependent sub-bands. For example, the *G* band intensity is orientation-dependent [143] and the *G* band can split into two sub-bands, G^+ and G^-, under uniaxial strains. The graphene crystallographic orientation can be then determined from these Raman characterizations.

4.1. G Band of Edge Chirality

The *G* Band Raman was proposed to identify the orientation of graphene edges [144]. The *G* band at edges exhibits obvious polarization dependence [34]. The Raman *G* band intensity is higher when the polarization direction of the incident laser is parallel to armchair edges or perpendicular to zigzag edges of graphene. Therefore, the orientation of the graphene edges can be identified using the intensity difference between armchair edges and zigzag edges. The orientation identification of whole graphene nanosheets can be concluded from the edge orientations.

Figure 9a shows typical Raman spectra of the *G* mode of an armchair edge under various polarization angles. The *G* band intensity increases with increasing polarization angles. This polarization dependence should result from the nature of the *G* mode in graphene, which has E_{2g} symmetry. On the contrary, the *G* mode intensity of the center region of graphene is not dependent on the polarization

direction, as shown in the inset in Figure 9a. So the polarization-dependent intensity of the *G* band can be normalized to the *G* band intensity of the whole graphene. Figure 9c shows the normalized polarization-dependent intensity of the *G* mode, indicating the polarization dependence of the *G* mode of the armchair edges.

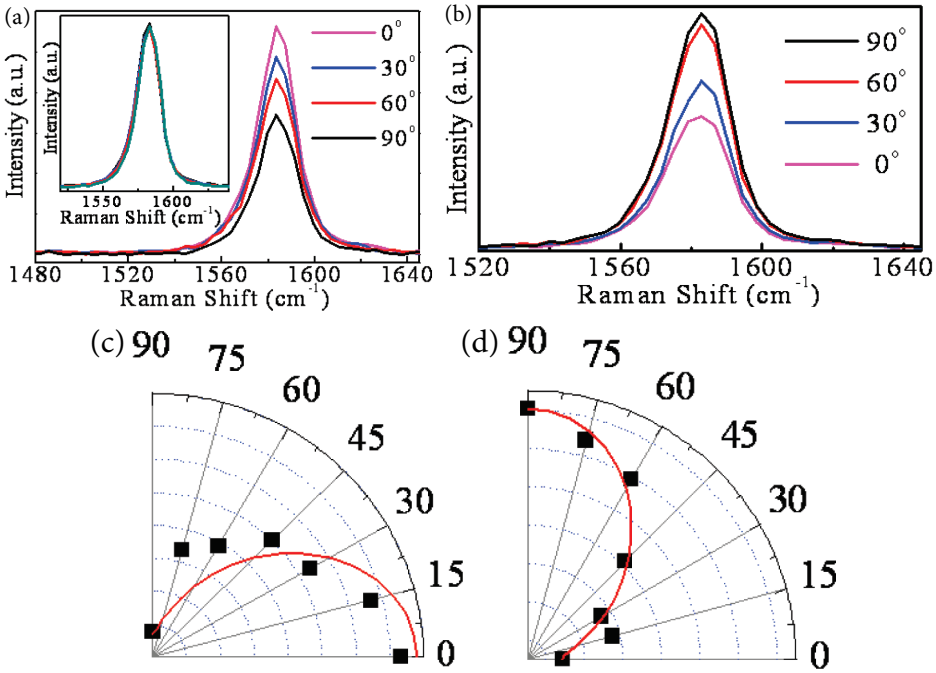

Figure 9. Raman *G* band of (**a**) armchair edges and (**b**) zigzag edges [34]. The polarization of the incident laser is 0°, 30°, 60°, and 90° with respect to the edges. Polar plots of the integrated intensity of the *G* mode at the (**c**) armchair-edges and (**d**) zigzag-edges [34]. The American Chemical Society.

The *G* band intensity shows different relationship along zigzag edges. Figure 9b shows the Raman *G* mode along zigzag edges. The intensity increases with increasing polarization angles. Figure 9d plots the normalized intensities of the *G* mode as a function of polar angles, indicating the polarization dependences of the *G* mode at zigzag-edges. Therefore, armchair edges and zigzag edges can be identified from the normalized polarization dependences of the *G* mode along edges [34].

4.2. G Band Splitting under Strain

The *G* band splits under strains. The strain-dependent splitting has been employed to detect the orientation of graphene nanosheets. Figure 10 shows typical Raman spectra under various strains. The *G* band red-shifts with increasing strain and the splitting gap increases with increasing strain. The splitting of the *G* band can reach up to 15 cm^{-1} under an applied strain of 1.3 % [57,58]. Additionally, the relative intensities of the G^+ sub-band and G^- sub-band are dependent on the laser polarization [58], providing useful information to detect graphene crystallographic orientations with respect to strains.

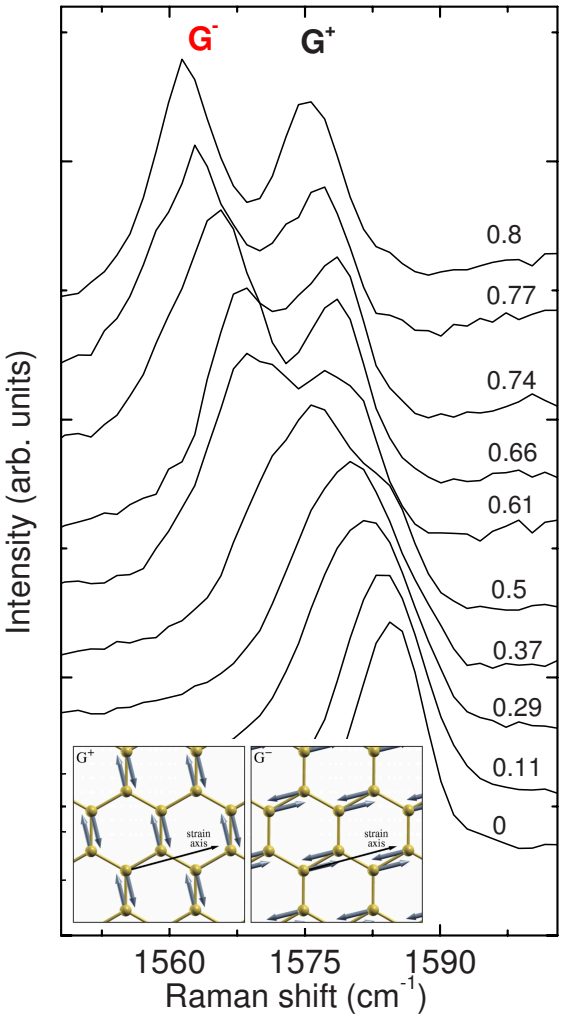

Figure 10. The G band as a function of uniaxial strain [58]. The spectra are collected with incident light polarized along the strain direction, collecting the scattered light with no analyzer. The strains are indicated, ranging from 0% to 0.8%. Inset: eigenvectors of two sub-bands G^+ and G^- modes split from the degenerate G band under strain. The American Physical Society.

Theoretically, the split G sub-bands are corresponding to two orthogonal modes respectively. One has eigenvectors perpendicular to the applied strain (E_{2g}^+) and the other parallel to the strain (E_{2g}^-), shown as the inset in Figure 10. When a uniaxial compressive strain is applied on graphene nanosheets, the sp^2 bonds parallel to the applied strain will be shortened and hardened. Other bonds perpendicular to the strains are only affected slightly. As a result, the G^- sub band, corresponding to the E_{2g}^- mode, is significantly shifted under the uniaxial strains. The G^+ sub band, corresponding to the E_{2g}^+ mode, is only moderately shifted under strains. Then the orientation of graphene can be experimentally probed from the intensity changes under strains.

In details, graphene nanosheets are strained and Raman spectra *in-situ* measured under different polarization directions. Figure 11a shows the G sub-bands at various incident laser polarizations under a strain. The sub-bands strongly depend on the laser polarization. The G^+ and G^- polar plots are shown in Figure 11b. The polar data can be fitted to $I_{G^+} \propto \sin^2(\theta_{in} + 34°)$ and $I_{G^+} \propto \cos^2(\theta_{in} + 34°)$. where θ_{in}, θ_{out}, and ϕ_s are illustrated in Figure 11c. The G^+ and G^- sub band intensity is strongest or weakest (Figure 11b) under certain polarization directions, whose angle θ_{in} between the strain direction can be experimental detected.

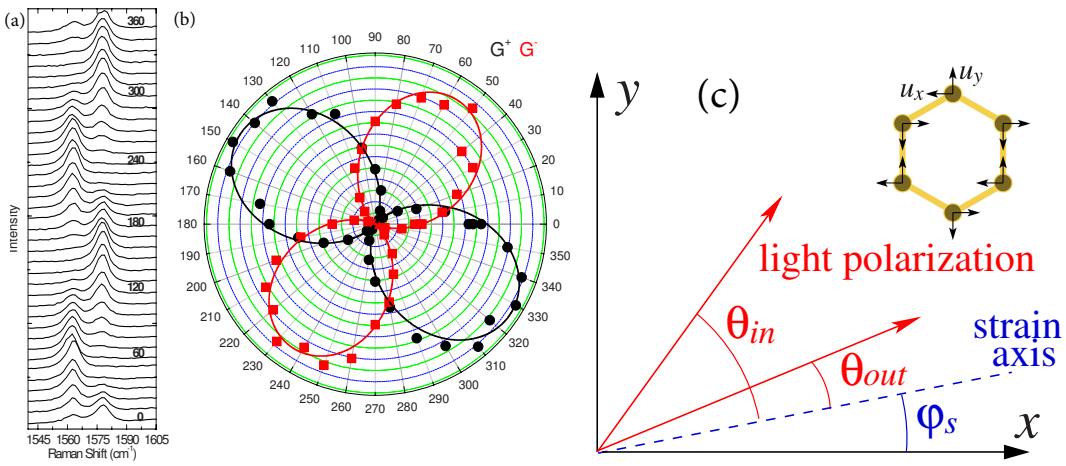

Figure 11. (**a**) Raman spectra and (**b**) polar plot of the fitted G^+ and G^- sub-bands as a function of the angle between the incident light polarization and the strain axis in measured with an analyzer selecting scattered polarization along the strain axis $\theta_{out} = 0°$ [58]. (**c**) Polarization geometry. The circles in the hexagon represent carbon atoms. The x axis is chosen perpendicular to the C-C bond. The short black arrows represent phonon displacements in the x, y basis. The American Physical Society.

The graphene crystallographic orientation can also be simply determined from the relative intensities of the G^+ and G^- sub-bands under uniaxial tensile strains [57,58,145]. The relative intensity of the G sub-bands is dependent on the angle (ϕ_s) between the strain axis and the graphene crystal axis [58]:

$$I_{G^-}/I_{G^+} = tan^2(\theta_{in} + \theta_{out} + 3\phi_s)$$

where I_{G^-} and I_{G^+} are the G sub-band intensities. Fitting the experimental data, the crystallographic orientation of the graphene crystal with respect to the known strain axis can be calculated.

4.3. 2D Band Splitting under Strain

Similarly, the $2D$ band can also be used to determine the orientation of graphene under uniaxial tension [145]. The $2D$ band red-shifts [58] and splits [75] under strains. The orientation of graphene can be determined from the strain-induced $2D$ band splitting.

Figure 12 shows the $2D$ band under strains along armchair and zigzag directions. Obviously, the $2D$ band splits into two sub-bands while red-shifts under strains. The splitting width increases with the increasing strain. The strain effect was observed by many groups [146] and explained as a deformation of the Dirac cone and a displacement away from the K point of the Brillouin zone.

The intensities of the $2D$ sub-bands show strong dependences on both incident and scattered laser polarization and graphene orientations [75,146]. Figure 13a shows the intensities of the $2D^-$ and $2D^+$ peaks measured as a function of the incident polarization angle θ_{in}. The analyzer is kept parallel to the incident polarization, $\theta_{in} = \theta_{out}$, which preferentially selects phonons in the direction orthogonal to θ_{in}. The polar plot of the sub-bands along armchair directions (Figure 13c) clearly indicates that the intensities of the $2D^-$ and $2D^+$ sub-band depend strongly on the polarization direction of the incident laser. The $2D$ sub-bands also show a strong dependence on orientations of zigzag edges under strains, as shown in Figure 13b,d. Therefore, the strain-induced splitting and red-shift of the $2D$ sub-bands can be used to detect the direction of graphene crystallographic orientations with respect to applied strains.

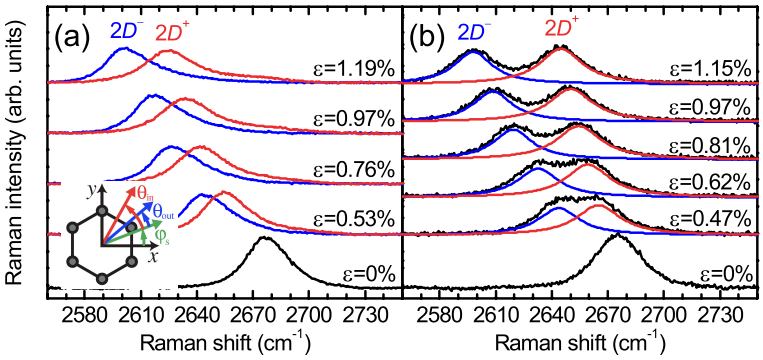

Figure 12. 2*D* sub-bands of graphene (**a**) strained along armchair edge with $\theta_{in} = \theta_{out} = 0°$ and (**b**) strained along zigzag-edge with $\theta_{in} = \theta_{out} = 90°$ under uniaxial strain ϵ [75]. The inset shows the polarization geometry. θ_{in}, θ_{out}, and ϕ_s are the angles that the incident laser polarization, the analyzer axis, and the zigzag direction make with respect to the strain axis, respectively. The American Physical Society.

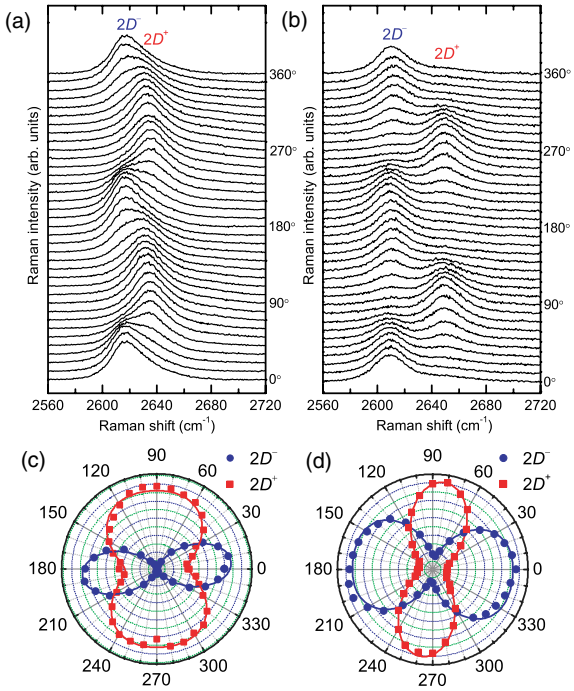

Figure 13. Evolutions of the 2*D* sub-bands of the (**a**) armchair-edge-strained and (**b**) zigzag-edge-strained graphene as a function of the incident laser polarization relative to the strain axis θ_{in}, under 0.97 % strain [75]. The analyzer is parallel to the incident laser polarization. Polar plots of the $2D^-$ and $2D^+$ bands of the (**c**) armchair-edge-strained and (**d**) zigzag-edge-strained graphene as a function of θ_{in}. The American Physical Society.

4.4. D Band of Edge Chirality

The *D* band is not split under uniaxial strain while shifts with hydrostatic stresses [58]. The armchair edge could be distinguished from the zigzag edge from the intensity of the *D* mode [43,147] because of the defect-assisted double resonant inter-valley scattering process. The details will not be discussed here as the intensity of the *D* band is usually very low for high-quality graphene with fewer defects.

As previously discussed, the *D* mode originates from a defect-assisted double resonance. Edges are one type of defects in graphene and their Raman spectroscopy has been investigated [97,140,148]. The Raman intensity of the *D* band depends on edge chirality. Theoretical studies of single-layer graphene indicated [60,100] that the double resonance process can only be fulfilled at an armchair edge (stronger *D* band) while for a zigzag edge, the resonance process is forbidden (weaker or vanished *D*

band). The *D* band intensity is localized mostly at the edges of the crystallite carbon nanomaterials [60]. Based on the theoretical prediction and experiments of graphite, many Raman *D* band mapping of edges have been reported [34,64,97,147]. It is found that the intensity of disorder-induced Raman *D* band (1350 cm^{-1}) is correlated to the edge chirality: it is stronger at the armchair edge and weaker at the zigzag edge. Therefore, the crystallographic orientation of graphene can be determined from the *D* band Raman mapping of edges.

4.4.1. *D* Band Raman Spectroscopy of Edges

Figure 14a plots the spectra of a graphene armchair edge under various incident laser polarizations. The *D* band intensity strongly depends on the angle between incident laser polarization and graphene edges. The *D* band intensity is maximum when the laser polarization direction is parallel to the edge and minimum when perpendicular to the edge. Figure 14b shows I_D / I_G as a function of θ_{in} for the edge. However, a detailed investigation showed that a perfect zigzag edge did not produce the *D* band [97]. Therefore, armchair edges and zigzag edges can be identified from the polarization-dependence *D* band intensity of edge chirality.

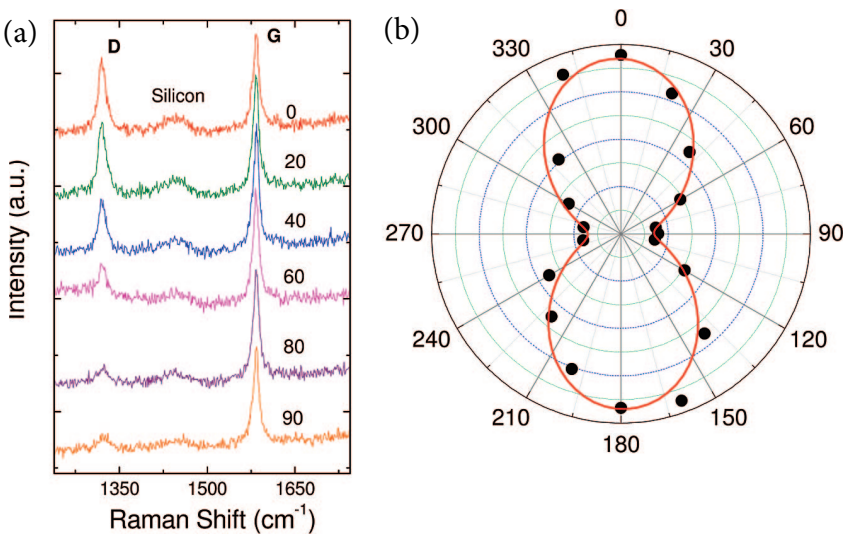

Figure 14. (**a**) Raman spectra of one edge measured for different incident polarization and (**b**) I_D / I_G as a function of θ_{in} [97]. The American Chemical Society.

The intensity of the *D* band is theoretically proportional to $[\vec{\mathbf{e}} \times \vec{\mathbf{p}}]$, where $\vec{\mathbf{e}}$ is the polarization of the incident laser, and $\vec{\mathbf{p}}$ is the momentum of the photo-excited electron or hole relative to the Dirac point. So, the *D* band intensity should be strongest when the polarization direction of the incident laser is parallel to armchair-edges. In details, the Raman intensity of the *D* band can be expressed as $I_D \propto \cos^2\theta_{in} \cos^2\theta_{out}$, where θ_{in} and θ_{out} are the angles of the incident and scattering electric fields relative to the graphene edges, respectively [34]. In other words, the *D* band is stronger near armchair edges and weaker near zigzag edges under certain conditions. Such kind of behavior can be employed to identify the edge chirality. Then, the crystallographic orientation of the whole graphene can be determined from the edge directions.

4.4.2. *D* Band Mapping of Edges

Figure 15 shows a single-layer graphene on Si substrates [34]. The angle between the polarization direction of the incident laser and graphene edges is 45°. The angle between the two edges is 90°. According to the morphology analysis of graphene in Section 2.2, the edge chirality of the two edges is different, one is armchair and one zigzag. The *G*-band Raman mapping (Figure 15b) can show the two edges of the graphene clearly which have same brightness whereas it cannot give any information

to identify the chirality of the edges. However, the *D* band mapping (Figure 15c), shows significant difference between the two edges. The Raman mapping is constructed from the spectra collected at the interior of the graphene and the edges. Clearly, the *D* band intensity is not uniform over the whole graphene. The disorder-induced *D* band is stronger at the vertical edge while very weak at the horizontal edge, suggesting the vertical edge is an armchair-edge and the horizontal edge is a zigzag-edge. Based on the fact that armchair-edges can scatter electrons near the Dirac points while zigzag-edges cannot, armchair edges and zigzag edges can be easily identified from *D* band mapping.

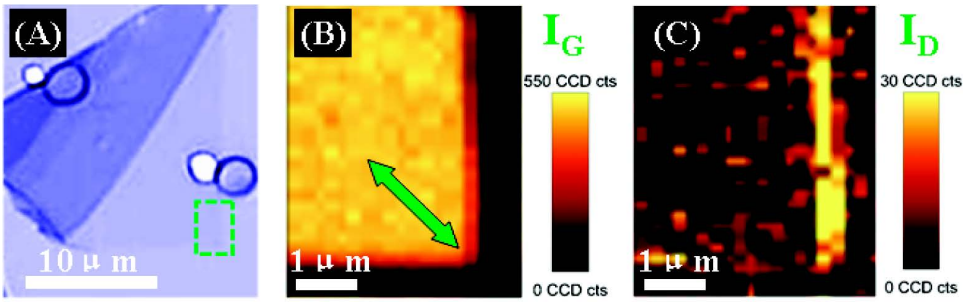

Figure 15. (**a**) Optical image of a single-layer graphene with two edges at 90° [34]. Raman images of the interested area highlighted in (**a**) by extracting the integrated intensity *G* band (**b**) and *D* band (**c**). The polarization of the incident laser is at 45° to each of the edges as illustrated. The American Chemical Society.

Several papers stated that it should be careful to conclude if a high *D* band intensity represents armchair edges or a low *D* band intensity stands for zigzag edges [64,97]. The given reasons are (1) Although the intensity of the *D* band strongly dependents on the polarization of incidence lasers, a minimum intensity of *D* band can also be detected when the angle between the laser polarization and graphene edge is 90°. (2) The measured *D* band intensity might come from both armchair edges and zigzag edges because of non-ideal edges of graphene and large laser beams. In one word, it can not determine armchair edges solely from higher *D* band intensity or higher I_D/I_G ratio.

In order to show the more detailed applications of *D* band mapping in graphene orientation, Figure 16 shows four single-layer graphenes with different chirality. The *D*-band Raman mapping was carried out on a confocal microscopy Raman system. The wavelength of the excitation laser was 532 nm. The Raman mapping images were collected by scanning the graphene nanosheets with a step of 100 nm with a spatial resolution 500 nm. For these graphene nanosheets with 30° and 90° angles (Figure 16a,c), the adjacent edges had different intensities of the *D* band (intensity ratio is greater than 1.6 for different edges chirality), which indicated that these two edges had different chirality. For the nanosheets with a 60° included angles (Figure 16b,d), two adjacent edges show similar *D* band intensity (intensity ratio is around 1.0), which means that they have the same atomic arrangements at the edges. From the Raman mapping images, the zigzag edges and armchair edges were identified.

Therefore, the edge chirality of graphene can be easily and nondestructively identified from the Raman *D* band mapping. The graphene orientations can be determined further from edge chiralities.

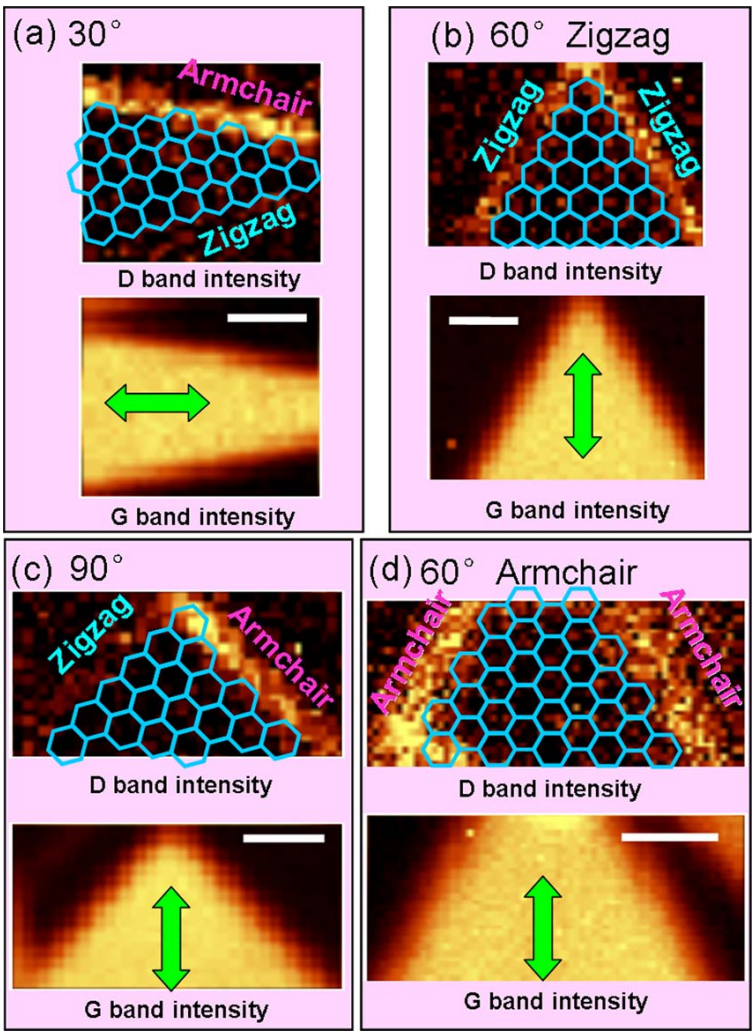

Figure 16. Raman imaging of the *D* band intensity of single-layer graphene edges with angles of (**a**) 30°, (**b**) 60° zigzag, (**c**) 90°, and (**d**) 60° armchair [147]. The images constructed by the *G* band intensity (bottom panels) show the positions and shapes of the single-layer graphene sheets. The laser polarization is indicated by the green arrows. The scale bar is 1 μm. The American Institute of Physics.

4.5. Extended Applications

In the previous sections, mechanical cleaved graphene nanosheets were utilized to demonstrate the Raman determination mechanisms. These discussed technologies are also valid to determine graphene nanosheets prepared by other methods. For example, the crystallographic orientation of CVD-grown graphene nanosheets was detected from the polarization dependence of Raman *G* band [149] and from Raman 2*D* band [150] (as shown in Figure 17a). Therefore, orientations of all kinds of graphene nanosheets can be characterized by these Raman technologies.

Recently, the discussed Raman techniques have also been employed to determine crystallographic orientations of other two-dimensional layered materials, such as MoS_2 [151,152], monolayer black phosphorus [6,8,142,153–155], atomically thin diselenide [156–161] and dichalcogenide [158,162,163], few-layer ditelluride [164,165], layered disulfide (ReS_2) [161], silicon films [139], pentacene films [166], heterostructures and hybrids [93], and other 2D materials [167]. Figure 17b–d show angle-resolved Raman intensities of black phosphorus, ReS_2, and $ReSe_2$ 2D layers, respectively. Orientation of these layers were identified from these polar plots.

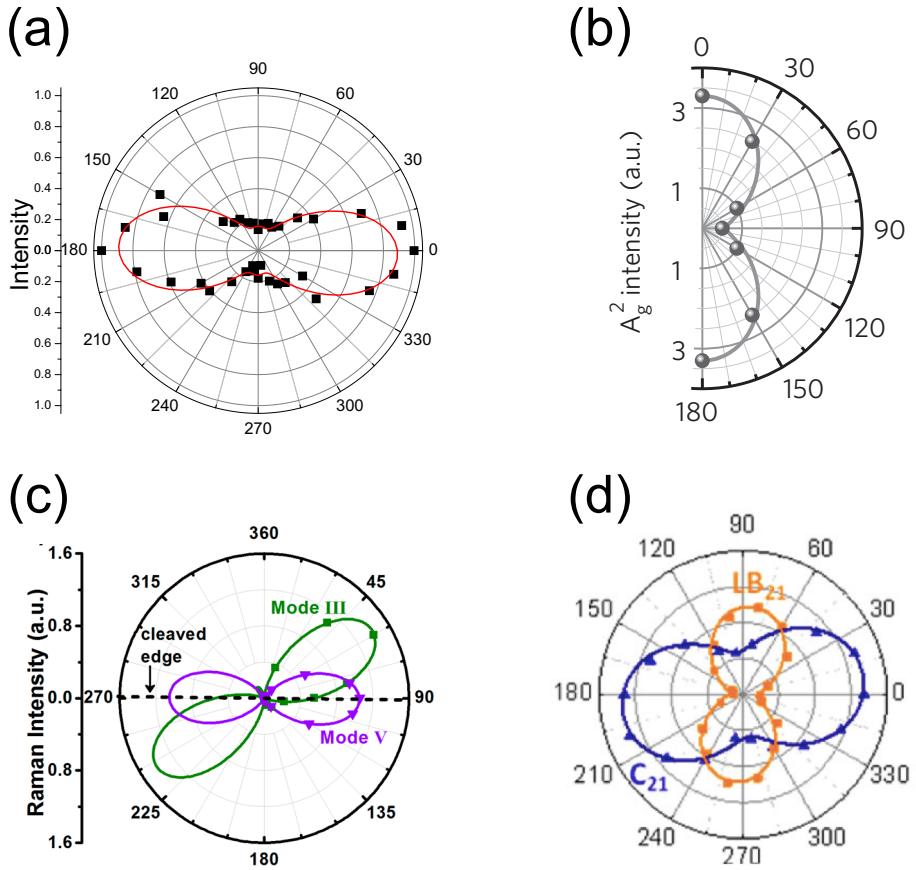

Figure 17. (**a**) I_{2D} intensity of CVD grown graphpene nanosheets on Cu substrates, as a function of the angle between the laser beam direction [150]. (**b**) Intensity of the A_g^2 Raman mode of monolayer black phosphorus as a function of the excitation laser polarization angle [8]. (**c**) Angle-resolved Raman intensities of two active modes of a ReS_2 layer [160]. (**d**) Polarization resolved Raman peak intensity of bilayer $ReSe_2$ [157].

Based on the wide applications of Raman techniques, it is reasonable to conclude that the Raman spectroscopy is a powerful tool to investigate 2*D* layered materials and will play more and more roles in orientation identification.

4.6. Comparison with Other Techniques

Besides Raman scattering, there are many other methods to detect orientation of graphene nanosheet, mainly including transmission electron microscopy (TEM), scanning electron microscopy (SEM), scanning tunneling microscopy (STM), atomic force microscopy (AFM), and various electron diffractions. Figure 18 shows several popular methods.

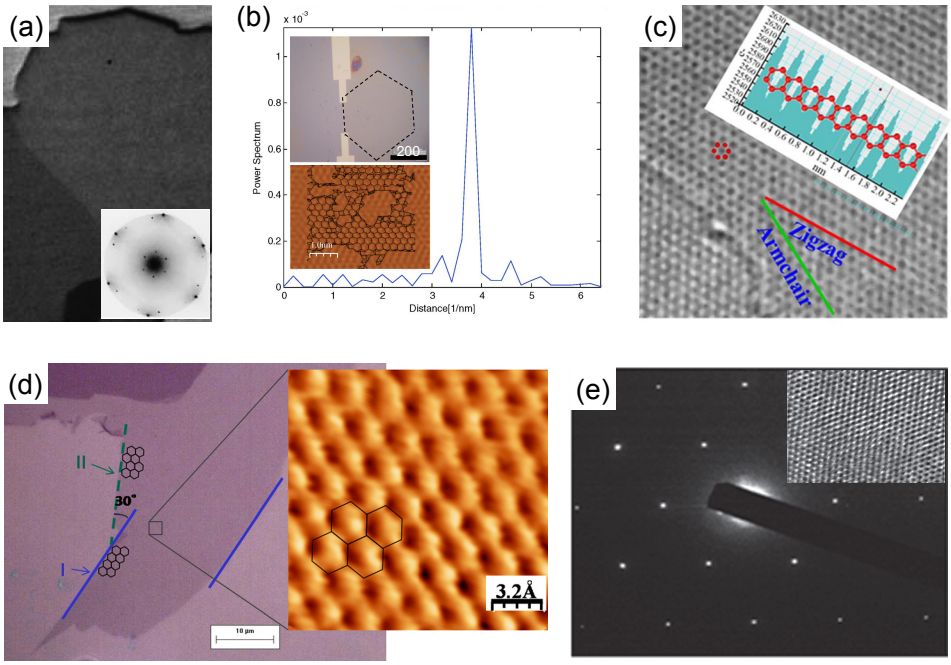

Figure 18. (**a**) LEEM image of graphene domains during temperature-controlled ripening [168]. Inset: LEED pattern of the dark domain. (**b**) Optical image of a grapheme and its spatial frequency power spectrum from a single friction scanning line [169]. The inset is an AFM image of the scanned region. (**c**) HRTEM image of a graphene [170]. Inset: line intensity profile of the red line. The distances between peaks are in agreement with the lattice spacing of graphene. (**d**) A lattice resolution AFM image of a graphene with its optical image with the highlighted two edges *I* and *II* [171]. (**e**) Selected-area electron diffraction pattern of graphene [38]. Inset: HRTEM image showing lattices.

Low-energy electron microscopy (LEEM) has been employed to in-situ investigate graphene rotated domains on Ir(111) substrates [168]. Figure 18a shows graphene domain grown on substrate grains. Selected-area low-energy electron diffraction (LEED) revealed that the orientation of domains rotated under high temperature because Moiré LEED spots are sensitive to domain orientation. The domain orientation relative to the Ir(111) lattice was identified by selected-area LEED within 0.5°.

Notably, a wavelet transform-based frequency identification method was developed to distinguish graphene orientation on AFM recently and lattice orientation can be determined through the different distribution of the frequency power spectrum just from a single scan line [169]. It was found that friction force signal varies with lattice orientation, having one peak along zigzag orientation and two peaks along armchair orientation. Based on the fact, the wavelet transform-based frequency can be used to identify graphene orientation. Figure 18b shows a spatial frequency spectrum of a single scanning line on a monolayer graphene (top inset). The one peak distribution indicated that the scanning line should be along the zigzag orientation. The detected orientation was consistent with an atomic resolution image (bottom inset). The method is simple and controllable while depends on the scanning quality of AFM.

Atomic-resolution AFM and TEM are visual methods to determine graphene orientation [37,39,45,170,171]. Figure 18c shows a lattice TEM image of graphene. Based on the lattice arrangements, the orientation of graphene can be directly characterized from images. Figure 18d shows a lattice resolution AFM image of a micromechanically exfoliated graphene on an oxidized Si substrate. The crystallographic orientation of the edge *I* was characterized as zigzag edge and *II* as armchair edge, as shown by the hexagons superimposing onto the optical image. The crystallographic orientations were in agreements with the results of Raman spectroscopy. These two methods are easy to identify edges while take time to obtain lattice images.

Additionally, high-resolution scanning tunneling microscopy (STM) has also been employed to detect graphene orientation [43,44]. Crystallographic orientation can be characterized directly from these atomic-resolution images.

Similar to LEED, selected area electron diffraction (SAED) is also a traditional method to determine crystallographic orientation [38–40]. Figure 18e shows an SAED pattern of graphene taken on TEM. Orientation of the graphene can be detected from the index of the pattern and the image rotation angle. Similar to electron diffractions, any FFT (Fast Fourier transform) patterns generated from lattice-resolution images (including HRTEM and AFM) can also be employed to detect crystallographic orientations.

Scanning electron microscopy [39,41] was also employed to characterize crystallographic orientation of graphene. Orientation can be characterized from graphene outlines. The method is simply while only works for CVD grown graphene on certain substrates.

Anisotropic optical absorption was employed to identify the crystalline orientation of black phosphorus [42]. It was stated that the optical method is more reliable and simple than Raman spectroscopy. The application of the technique on graphene is expected.

When comparing above techniques, there are no “good" or “bad" ones, nor someone is superior to the other ones. Instead, they all have advantages and disadvantages. The above discussed technologies can be classified into two categories, spectroscopy and microscopy. Raman spectroscopy lies in spectroscopy while TEM (including electron diffraction), SEM, STM and AFM are identified as microscopy. Spectroscopy (Raman) is based on photons, which can provide information as fine as molecular level, due to limitation of wavelength. Crystallographic orientation information is normally of atomic level. Thus, this piece of information has to be obtained through ratiocination, calculation and even experience based on Raman spectra. The advantage is that Raman require very little pre-treatment to samples. It is very easy to operate and time efficient (it normally takes seconds or milliseconds to acquire a Raman spectrum). Also, it is nondestructive to samples so that they can be used for future characterization, which is especially meaningful when the samples are valuable. Microscopy like TEM, SEM and STM, is based on electrons that is capable to unveil information at atomic level and output as visualizable images. This is direct observation of crystallographic orientation whereas the cost is time-consuming preparation of samples and operation of instruments. Moreover, the price of instruments varies depending on models and accessories to add, but normally electron microscopes (especially TEM) are much more expensive than Raman spectroscopes. The cost of instrumental maintenance and operation is also much higher for electron microscopes. AFM as a type of microscopes does not necessarily involve electron activity in the probe or scanning process. But the high resolution AFM can also achieve atomic level and provide surface information (atomic alignment) in the form of images.

5. Conclusions and Outlook

Raman spectroscopy has been widely utilized to characterize graphene, especially to determine crystallographic orientations of graphene using polarized Raman spectroscopy. Here, various determination principles are reviewed from physical properties of the D band, G band, and $2D$ band of graphene. The basic concepts are discussed and measurement procedures are sumarized. The techniques have great potentials in characterizations of crystallographic graphene orientations. Such kind of spectroscopic techniques will benefit the future explorations of orientation-dependent physical properties of two-dimensional graphene and other two-dimensional materials.

Acknowledgments: Y.C.L. is partially supported by the Army Research Laboratory under Cooperative Agreement Number W911NF-12-2-0022. The views and conclusions contained in this document are those of the authors and should not be interpreted as representing the official policies, either expressed or implied, of the Army Research Laboratory or the U.S. Government. The U.S. Government is authorized to reproduce and distribute reprints for Government purposes notwithstanding any copyright notation herein. A.L. is very thankful to the financial support from the National Science Foundation through research grant NSF DMR 1206380. C.W. acknowledges the Hubei “Chu-Tian Young Scholar” program.

Conflicts of Interest: The authors declare no conflict of interest.

References

1. Wang, Q.H.; Kalantar-Zadeh, K.; Kis, A.; Coleman, J.N.; Strano, M.S. Electronics and optoelectronics of two-dimensional transition metal dichalcogenides. *Nat. Nanotechnol.* **2012**, *7*, 699–712. [CrossRef] [PubMed]
2. Koppens, F.H.L.; Mueller, T.; Avouris, P.; Ferrari, A.C.; Vitiello, M.S.; Polini, M. Photodetectors based on graphene, other two-dimensional materials and hybrid systems. *Nat. Nanotechnol.* **2014**, *9*, 780–793. [CrossRef] [PubMed]
3. Fiori, G.; Bonaccorso, F.; Iannaccone, G.; Palacios, T.; Neumaier, D.; Seabaugh, A.; Banerjee, S.K.; Colombo, L. Electronics based on two-dimensional materials. *Nat. Nanotechnol.* **2014**, *9*, 768–779. [CrossRef] [PubMed]
4. Xia, F.; Wang, H.; Xiao, D.; Dubey, M.; Ramasubramaniam, A. Two-dimensional material nanophotonics. *Nat. Photonics* **2014**, *8*, 899–907. [CrossRef]
5. Chhowalla, M.; Shin, H.S.; Eda, G.; Li, L.J.; Loh, K.P.; Zhang, H. The chemistry of two-dimensional layered transition metal dichalcogenide nanosheets. *Nat. Chem.* **2013**, *5*, 263–275. [CrossRef] [PubMed]
6. Xia, F.; Wang, H.; Jia, Y. Rediscovering black phosphorus as an anisotropic layered material for optoelectronics and electronics. *Nat. Commun.* **2014**, *5*, 4458. [CrossRef] [PubMed]
7. Wu, J.; Mao, N.; Xie, L.; Xu, H.; Zhang, J. Identifying the crystalline orientation of black phosphorus using angle-resolved polarized Raman spectroscopy. *Angew. Chem.* **2015**, *127*, 2396–2399. [CrossRef]
8. Wang, X.; Jones, A.M.; Seyler, K.L.; Tran, V.; Jia, Y.; Zhao, H.; Wang, H.; Yang, L.; Xu, X.; Xia, F. Highly anisotropic and robust excitons in monolayer black phosphorus. *Nat. Nanotechnol.* **2015**, *10*, 517–521. [CrossRef] [PubMed]
9. Pakdel, A.; Zhi, C.; Bando, Y.; Golberg, D. Low-dimensional boron nitride nanomaterials. *Mater. Today* **2012**, *15*, 256–265. [CrossRef]
10. Li, L.H.; Chen, Y. Atomically thin boron nitride: Unique properties and applications. *Adv. Funct. Mater.* **2016**, *26*, 2594–2608. [CrossRef]
11. Mak, K.F.; Lee, C.; Hone, J.; Shan, J.; Heinz, T.F. Atomically thin MoS_2: A new direct-gap semiconductor. *Phys. Rev. Lett.* **2010**, *105*, 136805. [CrossRef] [PubMed]
12. Chuang, F.C.; Yao, L.Z.; Huang, Z.Q.; Liu, Y.T.; Hsu, C.H.; Das, T.; Lin, H.; Bansil, A. Prediction of Large-Gap Two-Dimensional Topological Insulators Consisting of Bilayers of Group III Elements with Bi. *Nano Lett.* **2014**, *14*, 2505–2508. [CrossRef] [PubMed]
13. Kou, L.; Ma, Y.; Sun, Z.; Heine, T.; Chen, C. Two-Dimensional Topological Insulators: Progress and Prospects. *J. Phys. Chem. Lett.* **2017**, *8*, 1905–1919. [CrossRef]
14. Wang, A.; Wang, C.; Fu, L.; Wong-Ng, W.; Lan, Y. Recent advances of graphitic carbon nitride-based structures and applications in catalyst, sensing, imaging, and LEDs. *Nano Micro Lett.* **2017**, *9*, 47. [CrossRef]
15. Mi, O.S.; Bandu, P.S.; Xiaoyan, J.; Seong-Ju, H. Recent Applications of 2D Inorganic Nanosheets for Emerging Energy Storage System. *Chem. A Eur. J.* **2017**, *24*, 4757–4773. [CrossRef]
16. Tan, C.; Cao, X.; Wu, X.J.; He, Q.; Yang, J.; Zhang, X.; Chen, J.; Zhao, W.; Han, S.; Nam, G.H.; et al. Recent advances in ultrathin two-dimensional nanomaterials. *Chem. Rev.* **2017**, *117*, 6225–6331. [CrossRef] [PubMed]
17. Kong, X.; Liu, Q.; Zhang, C.; Peng, Z.; Chen, Q. Elemental two-dimensional nanosheets beyond graphene. *Chem. Soc. Rev.* **2017**, *46*, 2127–2157. [CrossRef] [PubMed]
18. Neto, A.C.; Guinea, F.; Peres, N.M. Drawing conclusions from graphene. *Phys. World* **2006**, *19*, 33–37. [CrossRef]
19. Geim, A.K.; Novoselov, K.S. The rise of graphene. *Nat. Mater.* **2007**, *6*, 183–191. [CrossRef] [PubMed]
20. Novoselov, K.S.; Geim, A.K.; Morozov, S.V.; Jiang, D.; Zhang, Y.; Dubonos, S.V.; Grigorieva, I.V.; Firsov, A.A. Electric field effect in atomically thin carbon films. *Science* **2004**, *306*, 666–669. [CrossRef] [PubMed]
21. Novoselov, K.S.; Geim, A.K.; Morozov, S.V.; Jiang, D.; Katsnelson, M.I.; Grigorieva, I.V.; Dubonos, S.V.; Firsov, A.A. Two-dimensional gas of massless Dirac fermions in graphene. *Nature* **2005**, *438*, 197–200. [CrossRef] [PubMed]
22. Zhang, Y.; Tan, Y.W.; Stormer, H.L.; Kim, P. Experimental observation of the quantum Hall effect and Berry's phase in graphene. *Nature* **2005**, *438*, 201–204. [CrossRef] [PubMed]

23. Novoselov, K.S.; Jiang, Z.; Zhang, Y.; Morozov, S.V.; Stormer, H.L.; Zeitler, U.; Maan, J.C.; Boebinger, G.S.; Kim, P.; Geim, A.K. Room-temperature quantum Hall effect in graphene. *Science* **2007**, *315*, 1379. [CrossRef] [PubMed]
24. Heersche, H.B.; Jarillo-Herrero, P.; Oostinga, J.B.; Vandersypen, L.M.K.; Morpurgo, A.F. Bipolar supercurrent in graphene. *Nature* **2007**, *446*, 56–59. [CrossRef] [PubMed]
25. Ohta, T.; Bostwick, A.; Seyller, T.; Horn, K.; Rotenberg, E. Controlling the electronic structure of bilayer graphene. *Science* **2006**, *313*, 951–954. [CrossRef] [PubMed]
26. Meyer, J.C.; Geim, A.K.; Katsnelson, M.I.; Novoselov, K.S.; Booth, T.J.; Roth, S. The structure of suspended graphene sheets. *Nature* **2007**, *446*, 60–63. [CrossRef] [PubMed]
27. Trauzettel, B.; Bulaev, D.V.; Loss, D.; Burkard, G. Spin qubits in graphene quantum dots. *Nat. Phys.* **2007**, *3*, 192–196. [CrossRef]
28. Blake, P.; Brimicombe, P.D.; Nair, R.R.; Booth, T.J.; Jiang, D.; Schedin, F.; Ponomarenko, L.A.; Morozov, S.V.; Gleeson, H.F.; Hill, E.W.; et al. Graphene-based liquid crystal device. *Nano Lett.* **2008**, *8*, 1704–1708. [CrossRef] [PubMed]
29. Nair, R.R.; Blake, P.; Grigorenko, A.N.; Novoselov, K.S.; Booth, T.J.; Stauber, T.; Peres, N.M.R.; Geim, A.K. Fine structure constant defines visual transparency of graphene. *Science* **2008**, *320*, 1308. [CrossRef] [PubMed]
30. Balandin, A.A.; Ghosh, S.; Bao, W.; Calizo, I.; Teweldebrhan, D.; Miao, F.; Lau, C.N. Superior thermal conductivity of single-layer graphene. *Nano Lett.* **2008**, *8*, 902–907. [CrossRef] [PubMed]
31. Bunch, J.S.; van der Zande, A.M.; Verbridge, S.S.; Frank, I.W.; Tanenbaum, D.M.; Parpia, J.M.; Craighead, H.G.; McEuen, P.L. Electromechanical resonators from graphene sheets. *Science* **2007**, *315*, 490–493. [CrossRef] [PubMed]
32. Casiraghi, C.; Robertson, J.; Ferrari, A.C. Diamond-like carbon for data and beer storage. *Mater. Today* **2007**, *10*, 44–53. [CrossRef]
33. Sasaki, K.i.; Jiang, J.; Saito, R.; Onari, S.; Tanaka, Y. Theory of superconductivity of carbon nanotubes and graphene. *J. Phys. Soc. Jpn.* **2007**, *76*, 033702. [CrossRef]
34. Cong, C.; Yu, T.; Wang, H. Raman study on the G mode of graphene for determination of edge orientation. *ACS Nano* **2010**, *4*, 3175–3180. [CrossRef] [PubMed]
35. Nakada, K.; Fujita, M.; Dresselhaus, G.; Dresselhaus, M.S. Edge state in graphene ribbons: Nanometer size effect and edge shape dependence. *Phys. Rev. B* **1996**, *54*, 17954–17961. [CrossRef]
36. Abanin, D.A.; Lee, P.A.; Levitov, L.S. Charge and spin transport at the quantum Hall edge of graphene. *Solid State Commun.* **2007**, *143*, 77–85. [CrossRef]
37. Girit, C.O.; Meyer, J.C.; Erni, R.; Rossell, M.D.; Kisielowski, C.; Yang, L.; Park, C.H.; Crommie, M.F.; Cohen, M.L.; Louie, S.G.; et al. Graphene at the edge: Stability and dynamics. *Science* **2009**, *323*, 1705–1708. [CrossRef] [PubMed]
38. Dong, J.; Zeng, B.; Lan, Y.; Tian, S.; Shan, Y.; Liu, X.; Yang, Z.; Wang, H.; Ren, Z.F. Field emission from few-layer graphene nanosheets produced by liquid phase exfoliation of graphite. *J. Nanosci. Nanotechnol.* **2010**, *10*, 5051–5055. [CrossRef] [PubMed]
39. Murdock, A.T.; Koos, A.; Britton, T.B.; Houben, L.; Batten, T.; Zhang, T.; Wilkinson, A.J.; Dunin-Borkowski, R.E.; Lekka, C.E.; Grobert, N. Controlling the Orientation, Edge Geometry, and Thickness of Chemical Vapor Deposition Graphene. *ACS Nano* **2013**, *7*, 1351–1359. [CrossRef] [PubMed]
40. Zhao, H.; Lin, Y.C.; Yeh, C.H.; Tian, H.; Chen, Y.C.; Xie, D.; Yang, Y.; Suenaga, K.; Ren, T.L.; Chiu, P.W. Growth and Raman Spectra of Single-Crystal Trilayer Graphene with Different Stacking Orientations. *ACS Nano* **2014**, *8*, 10766–10773. [CrossRef] [PubMed]
41. Hu, J.; Xu, J.; Zhao, Y.; Shi, L.; Li, Q.; Liu, F.; Ullah, Z.; Li, W.; Guo, Y.; Liu, L. Roles of Oxygen and Hydrogen in Crystal Orientation Transition of Copper Foils for High-Quality Graphene Growth. *Sci. Rep.* **2017**, *7*, 45358. [CrossRef] [PubMed]
42. Ling, X.; Huang, S.; Hasdeo, E.H.; Liang, L.; Parkin, W.M.; Tatsumi, Y.; Nugraha, A.R.T.; Puretzky, A.A.; Das, P.M.; Sumpter, B.G.; et al. Anisotropic electron-photon and electron-phonon interactions in black phosphorus. *Nano Lett.* **2016**, *16*, 2260–2267. [CrossRef] [PubMed]
43. Cançado, L.G.; Pimenta, M.A.; Neves, B.R.A.; Dantas, M.S.S.; Jorio, A. Influence of the atomic structure on the Raman spectra of graphite edges. *Phys. Rev. Lett.* **2004**, *93*, 247401. [CrossRef]

44. Neubeck, S.; You, Y.M.; Ni, Z.H.; Blake, P.; Shen, Z.X.; Geim, A.K.; Novoselov, K.S. Direct determination of the crystallographic orientation of graphene edges by atomic resolution imaging. *Appl. Phys. Lett.* **2010**, *97*, 053110. [CrossRef]
45. Tang, S.; Wang, H.; Zhang, Y.; Li, A.; Xie, H.; Liu, X.; Liu, L.; Li, T.; Huang, F.; Xie, X.; Jiang, M. Precisely aligned graphene grown on hexagonal boron nitride by catalyst free chemical vapor deposition. *Sci. Rep.* **2013**, *3*, 2666. [CrossRef] [PubMed]
46. Reich, S.; Thomsen, C. Raman spectroscopy of graphite. *Phil. Trans. R. Soc. A Math. Phys. Eng. Sci.* **2004**, *362*, 2271–2288. [CrossRef] [PubMed]
47. Dresselhaus, M.S.; Eklund, P.C. Phonons in carbon nanotubes. *Adv. Phys.* **2000**, *49*, 705–814. [CrossRef]
48. Dresselhaus, M.; Dresselhaus, G.; Saito, R.; Jorio, A. Raman spectroscopy of carbon nanotubes. *Phys. Rep.* **2005**, *409*, 47–99. [CrossRef]
49. Ferrari, A.C.; Meyer, J.C.; Scardaci, V.; Casiraghi, C.; Lazzeri, M.; Mauri, F.; Piscanec, S.; Jiang, D.; Novoselov, K.S.; Roth, S.; et al. Raman spectrum of graphene and graphene layers. *Phys. Rev. Lett.* **2006**, *97*, 187401. [CrossRef] [PubMed]
50. Stampfer, C.; Molitor, F.; Graf, D.; Ensslin, K.; Jungen, A.; Hierold, C.; Wirtz, L. Raman imaging of doping domains in graphene on SiO_2. *Appl. Phys. Lett.* **2007**, *91*, 241907. [CrossRef]
51. Liu, L.; Ryu, S.; Tomasik, M.R.; Stolyarova, E.; Jung, N.; Hybertsen, M.S.; Steigerwald, M.L.; Brus, L.E.; Flynn, G.W. Graphene oxidation: thickness-dependent etching and strong chemical doping. *Nano Lett.* **2008**, *8*, 1965–1970. [CrossRef] [PubMed]
52. Das, A.; Pisana, S.; Chakraborty, B.; Piscanec, S.; Saha, S.K.; Waghmare, U.V.; Novoselov, K.S.; Krishnamurthy, H.R.; Geim, A.K.; Ferrari, A.C.; et al. Monitoring dopants by Raman scattering in an electrochemically top-gated graphene transistor. *Nat. Nanotechnol.* **2008**, *3*, 210–215. [CrossRef] [PubMed]
53. Luo, Z.; Yu, T.; Kim, K.-j.; Ni, Z.; You, Y.; Lim, S.; Shen, Z.; Wang, S.; Lin, J. Thickness-dependent reversible hydrogenation of graphene layers. *ACS Nano* **2009**, *3*, 1781–1788. [CrossRef] [PubMed]
54. Ni, Z.H.; Wang, H.M.; Kasim, J.; Fan, H.M.; Yu, T.; Wu, Y.H.; Feng, Y.P.; Shen, Z.X. Graphene thickness determination using reflection and contrast spectroscopy. *Nano Lett.* **2007**, *7*, 2758–2763. [CrossRef] [PubMed]
55. Graf, D.; Molitor, F.; Ensslin, K.; Stampfer, C.; Jungen, A.; Hierold, C.; Wirtz, L. Spatially resolved Raman spectroscopy of single- and few-layer graphene. *Nano Lett.* **2007**, *7*, 238–242. [CrossRef] [PubMed]
56. Mafra, D.L.; Samsonidze, G.; Malard, L.M.; Elias, D.C.; Brant, J.C.; Plentz, F.; Alves, E.S.; Pimenta, M.A. Determination of LA and TO phonon dispersion relations of graphene near the Dirac point by double resonance Raman scattering. *Phys. Rev. B* **2007**, *76*, 233407. [CrossRef]
57. Huang, M.; Yan, H.; Chen, C.; Song, D.; Heinz, T.F.; Hone, J. Phonon softening and crystallographic orientation of strained graphene studied by Raman spectroscopy. *Proc. Natl. Acad. Sci. USA* **2009**, *106*, 7304–7308. [CrossRef] [PubMed]
58. Mohiuddin, T.M.G.; Lombardo, A.; Nair, R.R.; Bonetti, A.; Savini, G.; Jalil, R.; Bonini, N.; Basko, D.M.; Galiotis, C.; Marzari, N.; et al. Uniaxial strain in graphene by Raman spectroscopy: *G* peak splitting, Grüneisen parameters, and sample orientation. *Phys. Rev. B* **2009**, *79*, 205433. [CrossRef]
59. Cançado, L.G.; Pimenta, M.A.; Saito, R.; Jorio, A.; Ladeira, L.O.; Grueneis, A.; Souza-Filho, A.G.; Dresselhaus, G.; Dresselhaus, M.S. Stokes and anti-Stokes double resonance Raman scattering in two-dimensional graphite. *Phys. Rev. B* **2002**, *66*, 035415. [CrossRef]
60. Pimenta, M.A.; Dresselhaus, G.; Dresselhaus, M.S.; Cancado, L.G.; Jorio, A.; Saito, R. Studying disorder in graphite-based systems by Raman spectroscopy. *Phys. Chem. Chem. Phys.* **2007**, *9*, 1276–1290. [CrossRef] [PubMed]
61. Yu, T.; Ni, Z.; Du, C.; You, Y.; Wang, Y.; Shen, Z. Raman mapping investigation of graphene on transparent flexible substrate: The strain effect. *J. Phys. Chem. C* **2008**, *112*, 12602–12605. [CrossRef]
62. Ni, Z.H.; Yu, T.; Lu, Y.H.; Wang, Y.Y.; Feng, Y.P.; Shen, Z.X. Uniaxial strain on graphene: Raman spectroscopy study and band-gap opening. *ACS Nano* **2008**, *2*, 2301–2305. [CrossRef] [PubMed]
63. Ferrari, A.C. Raman spectroscopy of graphene and graphite: Disorder, electron–phonon coupling, doping and nonadiabatic effects. *Solid State Commun.* **2007**, *143*, 47–57. [CrossRef]
64. Tang, B.; Guoxin, H.; Gao, H. Raman spectroscopic characterization of graphene. *Appl. Spectrosc. Rev.* **2010**, *45*, 369–407. [CrossRef]
65. Ni, Z.; Wang, Y.; Yu, T.; Shen, Z. Raman spectroscopy and imaging of graphene. *Nano Res.* **2008**, *1*, 273–291. [CrossRef]

66. Dresselhaus, M.S.; Jorio, A.; Saito, R. Characterizing graphene, graphite, and carbon nanotubes by Raman spectroscopy. *Annu. Rev. Condens. Matter Phys.* **2010**, *1*, 89–108. [CrossRef]
67. Malard, L.; Pimenta, M.; Dresselhaus, G.; Dresselhaus, M. Raman spectroscopy in graphene. *Phys. Rep.* **2009**, *473*, 51–87. [CrossRef]
68. Heller, E.J.; Yang, Y.; Kocia, L.; Chen, W.; Fang, S.; Borunda, M.; Kaxiras, E. Theory of graphene Raman scattering. *ACS Nano* **2016**, *10*, 2803–2818. [CrossRef] [PubMed]
69. Baskin, Y.; Meyer, L. Lattice constants of graphite at low temperatures. *Phys. Rev.* **1955**, *100*, 544–544. [CrossRef]
70. Vidano, R.P.; Fischbach, D.B.; Willis, L.J.; Loehr, T.M. Observation of Raman band shifting with excitation wavelength for carbons and graphites. *Solid State Commun.* **1981**, *39*, 341–344. [CrossRef]
71. Gupta, A.; Chen, G.; Joshi, P.; Tadigadapa, S. Raman scattering from high-frequency phonons in supported *n*-graphene layer films. *Nano Lett.* **2006**, *6*, 2667–2673. [CrossRef] [PubMed]
72. Jorio, A.; Saito, R.; Dresselhaus, G.; Dresselhaus, M.S. *Raman Spectroscopy in Graphene Related Systems*; Wiley-VCH Verlag GmbH & Co.: Weinheim, Germany, 2011. [CrossRef]
73. Ni, Z.H.; Wang, H.M.; Ma, Y.; Kasim, J.; Wu, Y.H.; Shen, Z.X. Tunable Stress and Controlled Thickness Modification in Graphene by Annealing. *ACS Nano* **2008**, *2*, 1033–1039. [CrossRef] [PubMed]
74. Calizo, I.; Balandin, A.A.; Bao, W.; Miao, F.; Lau, C.N. Temperature dependence of the Raman spectra of graphene and graphene multilayers. *Nano Lett.* **2007**, *7*, 2645–2649. [CrossRef] [PubMed]
75. Yoon, D.; Son, Y.W.; Cheong, H. Strain-dependent splitting of the double-resonance Raman scattering band in graphene. *Phys. Rev. Lett.* **2011**, *106*, 155502. [CrossRef]
76. Metzger, C.; Rémi, S.; Liu, M.; Kusminskiy, S.V.; Castro Neto, A.H.; Swan, A.K.; Goldberg, B.B. Biaxial Strain in Graphene Adhered to Shallow Depressions. *Nano Lett.* **2010**, *10*, 6–10. [CrossRef] [PubMed]
77. Yan, J.; Zhang, Y.; Kim, P.; Pinczuk, A. Electric field effect tuning of electron-phonon coupling in graphene. *Phys. Rev. Lett.* **2007**, *98*, 166802. [CrossRef] [PubMed]
78. Pisana, S.; Lazzeri, M.; Casiraghi, C.; Novoselov, K.S.; Geim, A.K.; Ferrari, A.C.; Mauri, F. Breakdown of the adiabatic Born–Oppenheimer approximation in graphene. *Nat. Mater.* **2007**, *6*, 198–201. [CrossRef] [PubMed]
79. Lee, J.E.; Ahn, G.; Shim, J.; Lee, Y.S.; Ryu, S. Optical separation of mechanical strain from charge doping in graphene. *Nat. Commun.* **2012**, *3*, 1024. [CrossRef] [PubMed]
80. Mueller, N.S.; Heeg, S.; na Alvarez, M.P.; Kusch, P.; Wasserroth, S.; Clark, N.; Schedin, F.; Parthenios, J.; Papagelis, K.; Galiotis, C.; et al. Evaluating arbitrary strain configurations and doping in graphene with Raman spectroscopy. *2D Materials* **2018**, *5*, 015016. [CrossRef]
81. Cançado, L.G.; Reina, A.; Kong, J.; Dresselhaus, M.S. Geometrical approach for the study of G′ band in the Raman spectrum of monolayer graphene, bilayer graphene, and bulk graphite. *Phys. Rev. Lett.* **2008**, *77*, 245408. [CrossRef]
82. Kürti, J.; Zólyomi, V.; Grüneis, A.; Kuzmany, H. Double resonant Raman phenomena enhanced by van Hove singularities in single-wall carbon nanotubes. *Phys. Rev. Lett.* **2002**, *65*, 165433. [CrossRef]
83. Thomsen, C.; Reich, S. Double resonant Raman scattering in graphite. *Phys. Rev. Lett.* **2000**, *85*, 5214–5217. [CrossRef] [PubMed]
84. Zólyomi, V.; Koltai, J.; Kürti, J. Resonance Raman spectroscopy of graphite and graphene. *Phys. Status Solidi B* **2011**, *248*, 2435–2444. [CrossRef]
85. Casiraghi, C.; Pisana, S.; Novoselov, K.S.; Geim, A.K.; Ferrari, A.C. Raman fingerprint of charged impurities in graphene. *Appl. Phys. Lett.* **2007**, *91*, 233108. [CrossRef]
86. Ding, F.; Ji, H.; Chen, Y.; Herklotz, A.; Dörr, K.; Mei, Y.; Rastelli, A.; Schmidt, O.G. Stretchable Graphene: A Close Look at Fundamental Parameters through Biaxial Straining. *Nano Lett.* **2010**, *10*, 3453–3458. [CrossRef] [PubMed]
87. Costa, S.D.; Righi, A.; Fantini, C.; Hao, Y.; Magnuson, C.; Colombo, L.; Ruoff, R.S.; Pimenta, M.A. Resonant Raman spectroscopy of graphene grown on copper substrates. *Solid State Commun.* **2012**, *152*, 1317–1320. [CrossRef]
88. Lee, D.S.; Riedl, C.; Krauss, B.; von Klitzing, K.; Starke, U.; Smet, J.H. Raman Spectra of Epitaxial Graphene on SiC and of Epitaxial Graphene Transferred to SiO_2. *Nano Lett* **2008**, *8*, 4320–4325. [CrossRef] [PubMed]
89. Tuinstra, F.; Koenig, J.L. Raman spectrum of graphite. *J. Chem. Phys.* **1970**, *53*, 1126–1130. [CrossRef]
90. Ferrari, A.C.; Robertson, J. Interpretation of Raman spectra of disordered and amorphous carbon. *Phys. Rev. B* **2000**, *61*, 14095–14107. [CrossRef]

91. Castiglioni, C.; Negri, F.; Rigolio, M.; Zerbi, G. Raman activation in disordered graphites of the A1′ symmetry forbidden $k \neq 0$ phonon: The origin of the D line. *J. Chem. Phys.* **2001**, *115*, 3769–3778. [CrossRef]
92. Lucchese, M.M.; Stavale, F.; Ferreira, E.H.M.; Vilani, C.; Moutinho, M.V.O.; Capaz, R.B.; Achete, C.A.; Jorio, A. Quantifying ion-induced defects and Raman relaxation length in graphene. *Carbon* **2010**, *48*, 1592–1597. [CrossRef]
93. Ferrari, A.C.; Basko, D.M. Raman spectroscopy as a versatile tool for studying the properties of graphene. *Nat. Nanotechnol.* **2013**, *8*, 235–246. [CrossRef] [PubMed]
94. Childres, I.; Jaureguib, L.A.; Park, W.; Cao, H.; Chen, Y.P. *Developments in Photon and Materials Research*; Chapter Raman Spectoscopy of Grphene and Related Materials; Nova Science Publishers, Development in Photon and Material Research: Hauppauge, NY, USA, 2013.
95. Beams, R.; Cançado, L.G.; Novotny, L. Raman characterization of defects and dopants in graphene. *J. Phys. Condens. Matter* **2015**, *27*, 083002. [CrossRef]
96. Sasaki, K.i.; Tokura, Y.; Sogawa, T. The origin of Raman D band: Bonding and antibonding orbitals in graphene. *Crystals* **2013**, *3*, 120–140. [CrossRef]
97. Casiraghi, C.; Hartschuh, A.; Qian, H.; Piscanec, S.; Georgi, C.; Fasoli, A.; Novoselov, K.S.; Basko, D.M.; Ferrari, A.C. Raman spectroscopy of graphene edges. *Nano Lett.* **2009**, *9*, 1433–1441. [CrossRef] [PubMed]
98. Basko, D.M. Boundary problems for Dirac electrons and edge-assisted Raman scattering in graphene. *Phys. Rev. B* **2009**, *79*, 205428. [CrossRef]
99. Katagiri, G.; Ishida, H.; Ishitani, A. Raman spectra of graphite edge planes. *Carbon* **1988**, *26*, 565–571. [CrossRef]
100. Cançado, L.G.; Pimenta, M.A.; Neves, B.R.A.; Medeiros-Ribeiro, G.; Enoki, T.; Kobayashi, Y.; Takai, K.; Fukui, K.i.; Dresselhaus, M.S.; Saito, R.; et al. Anisotropy of the Raman spectra of nanographite ribbons. *Phys. Rev. Lett.* **2004**, *93*, 047403. [CrossRef] [PubMed]
101. Eckmann, A.; Felten, A.; Verzhbitskiy, I.; Davey, R.; Casiraghi, C. Raman study on defective graphene: Effect of the excitation energy, type, and amount of defects. *Phys. Rev. B* **2013**, *88*, 035426. [CrossRef]
102. Mkhoyan, K.A.; Contryman, A.W.; Silcox, J.; Stewart, D.A.; Eda, G.; Mattevi, C.; Miller, S.; Chhowalla, M. Atomic and electronic structure of graphene-oxide. *Nano Lett.* **2009**, *9*, 1058–1063. [CrossRef] [PubMed]
103. Yan, J.A.; Xian, L.; Chou, M.Y. Structural and electronic properties of oxidized graphene. *Phys. Rev. Lett.* **2009**, *103*, 086802. [CrossRef] [PubMed]
104. Stankovich, S.; Piner, R.D.; Chen, X.; Wu, N.; Nguyen, S.T.; Ruoff, R.S. Stable aqueous dispersions of graphitic nanoplatelets via the reduction of exfoliated graphite oxide in the presence of poly(sodium 4-styrenesulfonate). *J. Mater. Chem.* **2006**, *16*, 155–158. [CrossRef]
105. Chen, D.; Feng, H.; Li, J. Graphene oxide: Preparation, functionalization, and electrochemical applications. *Chem. Rev.* **2012**, *112*, 6027–6053. [CrossRef] [PubMed]
106. Feng, W.; Long, P.; Feng, Y.; Li, Y. Two-dimensional fluorinated graphene: synthesis, structures, properties and applications. *Adv. Sci.* **2015**, *3*, 1500413. [CrossRef] [PubMed]
107. Sofo, J.O.; Chaudhari, A.S.; Barber, G.D. Graphane: A two-dimensional hydrocarbon. *Phys. Rev. B* **2007**, *75*, 153401. [CrossRef]
108. Karlický, F.; Kumara Ramanatha Datta, K.; Otyepka, M.; Zbořil, R. Halogenated graphenes: Rapidly growing family of graphene derivatives. *ACS Nano* **2013**, *7*, 6434–6464. [CrossRef] [PubMed]
109. Leenaerts, O.; Peelaers, H.; Hernández-Nieves, A.D.; Partoens, B.; Peeters, F.M. First-principles investigation of graphene fluoride and graphane. *Phys. Rev. B* **2010**, *82*, 195436. [CrossRef]
110. Muñoz, E.; Singh, A.K.; Ribas, M.A.; Penev, E.S.; Yakobson, B.I. The ultimate diamond slab: GraphAne versus graphEne. *Diam. Relat. Mater.* **2010**, *19*, 368–373. [CrossRef]
111. Kudin, K.N.; Ozbas, B.; Schniepp, H.C.; Prud'homme, R.K.; Aksay, I.A.; Car, R. Raman spectra of graphite oxide and functionalized graphene sheets. *Nano Lett* **2008**, *8*, 36–41. [CrossRef] [PubMed]
112. Allen, M.J.; Tung, V.C.; Kaner, R.B. Honeycomb carbon: A review of graphene. *Chem. Rev.* **2010**, *110*, 132–145. [CrossRef] [PubMed]
113. Bonaccorso, F.; Lombardo, A.; Hasan, T.; Sun, Z.; Colombo, L.; Ferrari, A.C. Production and processing of graphene and 2D crystals. *Mater. Today* **2012**, *15*, 564–589. [CrossRef]
114. Novoselov, K.S.; Jiang, D.; Schedin, F.; Booth, T.J.; Khotkevich, V.V.; Morozov, S.V.; Geim, A.K. Two-dimensional atomic crystals. *Proc. Natl. Acad. Sci. USA* **2005**, *102*, 10451–10453. [CrossRef] [PubMed]

115. Berger, C.; Song, Z.; Li, T.; Li, X.; Ogbazghi, A.Y.; Feng, R.; Dai, Z.; Marchenkov, A.N.; Conrad, E.H.; First, P.N.; et al. Ultrathin epitaxial graphite: 2D electron gas properties and a route toward graphene-based nanoelectronics. *J. Phys. Chem. B* **2004**, *108*, 19912–19916. [CrossRef]
116. Berger, C.; Song, Z.; Li, X.; Wu, X.; Brown, N.; Naud, C.; Mayou, D.; Li, T.; Hass, J.; Marchenkov, A.N.; et al. Electronic confinement and coherence in patterned epitaxial graphene. *Science* **2006**, *312*, 1191–1196. [CrossRef] [PubMed]
117. Dedkov, Y.S.; Fonin, M.; Rüdiger, U.; Laubschat, C. Rashba effect in the graphene/Ni(111) system. *Phys. Rev. Lett.* **2008**, *100*, 107602. [CrossRef] [PubMed]
118. Hernandez, Y.; Nicolosi, V.; Lotya, M.; Blighe, F.M.; Sun, Z.; De, S.; McGovern, I.T.; Holland, B.; Byrne, M.; Gun'Ko, Y.K.; et al. High-yield production of graphene by liquid-phase exfoliation of graphite. *Nature Nanotechnol.* **2008**, *3*, 563. [CrossRef] [PubMed]
119. Li, X.; Wang, X.; Zhang, L.; Lee, S.; Dai, H. Chemically derived, ultrasmooth graphene nanoribbon semiconductors. *Science* **2008**, *319*, 1229–1232. [CrossRef] [PubMed]
120. Li, D.; Müller, M.B.; Gilje, S.; Kaner, R.B.; Wallace, G.G. Processable aqueous dispersions of graphene nanosheets. *Nat. Nanotechnol.* **2008**, *3*, 101–105. [CrossRef] [PubMed]
121. Stankovich, S.; Dikin, D.A.; Dommett, G.H.B.; Kohlhaas, K.M.; Zimney, E.J.; Stach, E.A.; Piner, R.D.; Nguyen, S.T.; Ruoff, R.S. Graphene-based composite materials. *Nature* **2006**, *442*, 282. [CrossRef] [PubMed]
122. Khan, U.; O'Neill, A.; Lotya, M.; De, S.; Coleman, J.N. High-Concentration Solvent Exfoliation of Graphene. *Small* **2010**, *6*, 864–871. [CrossRef] [PubMed]
123. Su, C.Y.; Lu, A.Y.; Xu, Y.; Chen, F.R.; Khlobystov, A.N.; Li, L.J. High-Quality Thin Graphene Films from Fast Electrochemical Exfoliation. *ACS Nano* **2011**, *5*, 2332–2339. [CrossRef] [PubMed]
124. Wang, J.; Manga, K.K.; Bao, Q.; Loh, K.P. High-Yield Synthesis of Few-Layer Graphene Flakes through Electrochemical Expansion of Graphite in Propylene Carbonate Electrolyte. *J. Am. Chem. Soc.* **2011**, *133*, 8888–8891. [CrossRef] [PubMed]
125. Cooper, A.J.; Wilson, N.R.; Kinloch, I.A.; Dryfe, R.A. Single stage electrochemical exfoliation method for the production of few-layer graphene via intercalation of tetraalkylammonium cations. *Carbon* **2014**, *66*, 340–350. [CrossRef]
126. Parvez, K.; Wu, Z.S.; Li, R.; Liu, X.; Graf, R.; Feng, X.; Müllen, K. Exfoliation of Graphite into Graphene in Aqueous Solutions of Inorganic Salts. *J. Am. Chem. Soc.* **2014**, *136*, 6083–6091. [CrossRef] [PubMed]
127. Blake, P.; Hill, E.W.; Neto, A.H.C.; Novoselov, K.S.; Jiang, D.; Yang, R.; Booth, T.J.; Geim, A.K. Making graphene visible. *Appl. Phys. Lett.* **2007**, *91*, 063124. [CrossRef]
128. Jung, I.; Pelton, M.; Piner, R.; Dikin, D.A.; Stankovich, S.; Watcharotone, S.; Hausner, M.; Ruoff, R.S. Simple approach for high-contrast optical imaging and characterization of graphene-based sheets. *Nano Lett.* **2007**, *7*, 3569–3575. [CrossRef]
129. Casiraghi, C.; Hartschuh, A.; Lidorikis, E.; Qian, H.; Harutyunyan, H.; Gokus, T.; Novoselov, K.S.; Ferrari, A.C. Rayleigh imaging of graphene and graphene layers. *Nano Lett.* **2007**, *7*, 2711–2717. [CrossRef] [PubMed]
130. Abergel, D.S.L.; Russell, A.; Fal'ko, V.I. Visibility of graphene flakes on a dielectric substrate. *Appl. Phys. Lett.* **2007**, *91*, 063125. [CrossRef]
131. Roddaro, S.; Pingue, P.; Piazza, V.; Pellegrini, V.; Beltram, F. The optical visibility of graphene: Interference colors of ultrathin graphite on SiO_2. *Nano Lett.* **2007**, *7*, 2707–2710. [CrossRef] [PubMed]
132. Koskinen, P.; Malola, S.; Häkkinen, H. Evidence for graphene edges beyond zigzag and armchair. *Phys. Rev. B* **2009**, *80*, 073401. [CrossRef]
133. He, R.; Yan, J.A.; Yin, Z.; Ye, Z.; Ye, G.; Cheng, J.; Li, J.; Lui, C.H. Coupling and stacking order of ReS_2 atomic layers revealed by ultralow-frequency Raman spectroscopy. **2016**, *16*, 1404–1409. [CrossRef] [PubMed]
134. Nagler, P.; Plechinger, G.; Schüller, C.; Korn, T. Observation of anisotropic interlayer Raman modes in few-layer ReS_2. *Rapid Res. Lett.* **2016**, *10*, 185–189. [CrossRef]
135. Sevinçli, H.; Topsakal, M.; Ciraci, S. *Low Dimensional Semiconductor Structures*; Chapter Functionalization of Graphene Nanoribbons; Springer: Berlin, Germany, 2013.
136. Hopkins, J.B.; Farrow, L.A.; Fisanick, G.J. Raman microprobe determination of local crystal orientation in laser annealed silicon. *Appl. Phys. Lett.* **1984**, *44*, 535–537. [CrossRef]
137. Hopkins, J.B.; Farrow, L.A. Raman microprobe determination of local crystal orientation. *J. Appl. Phys.* **1986**, *59*, 1103–1110. [CrossRef]

138. Nakashima, S.-i.; Mizoguchi, K.; Inoue, Y.; Miyauchi, M.; Mitsuishi, A.; Nishimura, T.; Akasaka, Y. Raman image measurements of laser-recrystallized polycrystalline Si films by a scanning Raman microprobe. *Jpn. J. Appl. Phys.* **1986**, *25*, L222–L224. [CrossRef]
139. Mizoguchi, K.; Nakashima, S. Determination of crystallographic orientations in silicon films by Raman-microprobe polarization measurements. *J. Appl. Phys.* **1989**, *65*, 2583–2590. [CrossRef]
140. Yoon, D.; Moon, H.; Son, Y.W.; Samsonidze, G.; Park, B.H.; Kim, J.B.; Lee, Y.; Cheong, H. Strong polarization dependence of double-resonant Raman intensities in graphene. *Nano Lett.* **2008**, *8*, 4270–4274. [CrossRef] [PubMed]
141. Heo, G.; Kim, Y.S.; Chun, S.H.; Seong, M.J. Polarized Raman spectroscopy with differing angles of laser incidence on single-layer graphene. *Nanoscale Res. Lett.* **2015**, *10*, 45. [CrossRef] [PubMed]
142. Kim, J.; Lee, J.U.; Lee, J.; Park, H.J.; Lee, Z.; Lee, C.; Cheong, H. Anomalous polarization dependence of Raman scattering and crystallographic orientation of black phosphorus. *Nanoscale* **2015**, *7*, 18708–18715. [CrossRef] [PubMed]
143. Kim, K.; Coh, S.; Tan, L.Z.; Regan, W.; Yuk, J.M.; Chatterjee, E.; Crommie, M.F.; Cohen, M.L.; Louie, S.G.; Zettl, A. Raman spectroscopy study of rotated double-layer graphene: misorientation-angle dependence of electronic structure. *Phys. Rev. Lett.* **2012**, *108*, 246103. [CrossRef] [PubMed]
144. Sasaki, K.i.; Saito, R.; Wakabayashi, K.; Enoki, T. Identifying the orientation of edge of graphene using G band Raman spectra. *J. Phys. Soc. Jpn.* **2010**, *79*, 044603. [CrossRef]
145. Frank, O.; Mohr, M.; Maultzsch, J.; Thomsen, C.; Riaz, I.; Jalil, R.; Novoselov, K.S.; Tsoukleri, G.; Parthenios, J.; Papagelis, K.; et al. Raman 2D-band splitting in graphene: theory and experiment. *ACS Nano* **2011**, *5*, 2231–2239. [CrossRef] [PubMed]
146. Huang, M.; Yan, H.; Heinz, T.F.; Hone, J. Probing strain-induced electronic structure change in graphene by Raman spectroscopy. *Nano Lett.* **2010**, *10*, 4074–4079. [CrossRef] [PubMed]
147. You, Y.; Ni, Z.; Yu, T.; Shen, Z. Edge chirality determination of graphene by Raman spectroscopy. *Appl. Phys. Lett.* **2008**, *93*, 163112. [CrossRef]
148. Gupta, A.K.; Russin, T.J.; Gutiérrez, H.R.; Eklund, P.C. Probing graphene edges via Raman scattering. *ACS Nano* **2009**, *3*, 45–52. [CrossRef] [PubMed]
149. Jegal, S.; Hao, Y.; Yoon, D.; Ruoff, R.S.; Yun, H.; Lee, S.W.; Cheong, H. Crystallographic orientation of early domains in CVD graphene studied by Raman spectroscopy. *Chem. Phys. Lett.* **2013**, *568–569*, 146–150. [CrossRef]
150. Li, Z.; Young, R.J.; Kinloch, I.A.; Wilson, N.R.; Marsden, A.J.; Raju, A.P.A. Quantitative determination of the spatial orientation of graphene by polarized Raman spectroscopy. *Carbon* **2015**, *88*, 215–224. [CrossRef]
151. Lee, C.; Yan, H.; Brus, L.E.; Heinz, T.F.; Hone, J.; Ryu, S. Anomalous lattice vibrations of single- and few-layer MoS_2. *ACS Nano* **2010**, *4*, 2695–2700. [CrossRef] [PubMed]
152. Doratotaj, D.; Simpson, J.R.; Yan, J.A. Probing the uniaxial strains in MoS_2 using polarized Raman spectroscopy: A first-principles study. *Phys. Rev. B* **2016**, *93*, 075401. [CrossRef]
153. Zhang, S.; Yang, J.; Xu, R.; Wang, F.; Li, W.; Ghufran, M.; Zhang, Y.W.; Yu, Z.; Zhang, G.; Qin, Q.; Lu, Y. Extraordinary photoluminescence and strong temperature/angle-dependent Raman responses in few-layer phosphorene. *ACS Nano* **2014**, *8*, 9590–9596. [CrossRef] [PubMed]
154. Juanxia, W.; Nannan, M.; Liming, X.; Hua, X.; Jin, Z. Identifying the crystalline orientation of black phosphorus using angle-resolved polarized Raman spectroscopy. *Angew. Chem. Int. Ed.* **2015**, *54*, 2366–2369. [CrossRef]
155. Ribeiro, H.B.; Pimenta, M.A.; de Matos, C.J.S.; Moreira, R.L.; Rodin, A.S.; Zapata, J.D.; de Souza, E.A.T.; Castro Neto, A.H. Unusual angular dependence of the Raman response in black phosphorus. *ACS Nano* **2015**, *9*, 4270–4276. [CrossRef] [PubMed]
156. Del Corro, E.; Terrones, H.; Elias, A.; Fantini, C.; Feng, S.; Nguyen, M.A.; Mallouk, T.E.; Terrones, M.; Pimenta, M.A. Excited excitonic states in 1L, 2L, 3L, and bulk WSe_2 observed by resonant Raman spectroscopy. *ACS Nano* **2014**, *8*, 9629–9635. [CrossRef] [PubMed]
157. Zhao, H.; Wu, J.; Zhong, H.; Guo, Q.; Wang, X.; Xia, F.; Yang, L.; Tan, P.; Wang, H. Interlayer interactions in anisotropic atomically thin rhenium diselenide. *Nano Res.* **2015**, *8*, 3651–3661. [CrossRef]
158. Chen, S.Y.; Zheng, C.; Fuhrer, M.S.; Yan, J. Helicity-resolved Raman scattering of MoS_2, $MoSe_2$, WS_2, and WSe_2 atomic layers. *Nano Lett.* **2015**, *15*, 2526–2532. [CrossRef] [PubMed]
159. Wolverson, D.; Crampin, S.; Kazemi, A.S.; Ilie, A.; Bending, S.J. Raman spectra of monolayer, few-Layer, and bulk $ReSe_2$: An anisotropic layered semiconductor. *ACS Nano* **2014**, *8*, 11154–11164. [CrossRef] [PubMed]

160. Chenet, D.A.; Aslan, O.B.; Huang, P.Y.; Fan, C.; van der Zande, A.M.; Heinz, T.F.; Hone, J.C. In-plane anisotropy in mono- and few-layer ReS_2 probed by Raman spectroscopy and scanning transmission electron microscopy. *Nano Lett.* **2015**, *15*, 5667–5672. [CrossRef] [PubMed]
161. Lorchat, E.; Froehlicher, G.; Berciaud, S. Splitting of interlayer shear modes and photon energy dependent anisotropic Raman response in *n*-layer $ReSe_2$ and ReS_2. *ACS Nano* **2016**, *10*, 2752–2760. [CrossRef] [PubMed]
162. Puretzky, A.A.; Liang, L.; Li, X.; Xiao, K.; Wang, K.; Mahjouri-Samani, M.; Basile, L.; Idrobo, J.C.; Sumpter, B.G.; Meunier, V.; Geohegan, D.B. Low-frequency Raman fingerprints of two-dimensional metal dichalcogenide layer stacking configurations. *ACS Nano* **2015**, *9*, 6333–6342. [CrossRef] [PubMed]
163. O'Brien, M.; McEvoy, N.; Hanlon, D.; Hallam, T.; Coleman, J.N.; Duesberg, G.S. Mapping of Low-Frequency Raman Modes in CVD-Grown Transition Metal Dichalcogenides: Layer Number, Stacking Orientation and Resonant Effects. *Phys. Rev. B* **2016**, *6*, 19476. [CrossRef] [PubMed]
164. Kim, M.; Han, S.; Kim, J.H.; Lee, J.U.; Lee, Z.; Cheong, H. Determination of the thickness and orientation of few-layer tungsten ditelluride using polarized Raman spectroscopy. *2D Materials* **2016**, *3*, 034004. [CrossRef]
165. Wang, J.; Luo, X.; Li, S.; Verzhbitskiy, I.; Zhao, W.; Wang, S.; Quek, S.Y.; Eda, G. Determination of crystal axes in semimetallic T′-$MoTe_2$ by polarized Raman spectroscopy. *Adv. Funct. Mater.* **2017**, *27*, 1604799. [CrossRef]
166. Chen, C.Y.; Wong, D.P.; Huang, Y.F.; Lien, H.T.; Chiang, P.C.; Li, P.L.; Shih, F.Y.; Wang, W.H.; Chen, K.H.; Chen, L.C.; et al. Understanding the Interplay between Molecule Orientation and Graphene Using Polarized Raman Spectroscopy. *ACS Photonics* **2016**, *3*, 985–991. [CrossRef]
167. Zhang, X.; Tan, Q.H.; Wu, J.B.; Shi, W.; Tan, P.H. Review on the Raman spectroscopy of different types of layered materials. *Nanoscale* **2016**, *8*, 6435–6450. [CrossRef] [PubMed]
168. Rogge, P.C.; Thürmer, K.; Foster, M.E.; McCarty, K.F.; Dubon, O.D.; Bartelt, N.C. Real-time observation of epitaxial graphene domain reorientation. *Nat. Commun.* **2015**, *6*, 6880. [CrossRef] [PubMed]
169. Zhang, Y.; Yu, F.; Li, G.; Liu, L.; Liu, G.; Zhang, Z.; Wang, Y.; Wejinya, U.C.; Xi, N. Online Determination of Graphene Lattice Orientation Through Lateral Forces. *Nanoscale Res. Lett.* **2016**, *11*, 353. [CrossRef] [PubMed]
170. Cong, C.; Li, K.; Zhang, X.X.; Yu, T. Visualization of arrangements of carbon atoms in graphene layers by Raman mapping and atomic-resolution TEM. *Sci. Rep.* **2013**, *3*, 1195. [CrossRef] [PubMed]
171. Almeida, C.M.; Carozo, V.; Prioli, R.; Achete, C.A. Identification of graphene crystallographic orientation by atomic force microscopy. *J. Appl. Phys.* **2011**, *110*, 086101. [CrossRef]